Magnetic and atomic short range order in Fe1−xCrx alloys

I. Mirebeau, V. Pierron-Bohnes, C. Decorse, E. Rivière, Chu-Chun Fu, Kangming Li, G. Parette, N. Martin

Magnetic and atomic short range order in $Fe_{1-x}Cr_x$ alloys

I. Mirebeau,[1] V. Pierron-Bohnes,[2] C. Decorse,[3] E. Rivière,[3] Chu-Chun Fu,[4] Kangming Li,[4] G. Parette,[1] and N. Martin[1]

[1]*Laboratoire Léon Brillouin, CEA-CNRS, Université Paris-Saclay, CEA-Saclay, F-91191 Gif-sur-Yvette, France*

[2]*Université de Strasbourg, CNRS, Institut de Physique et Chimie des Matériaux de Strasbourg (IPCMS), UMR 7504, F-67000 Strasbourg, France*

[3]*ICMMO, Université Paris-Sud, Université Paris-Saclay, F-91405 Orsay, France*

[4]*DEN-Service de Recherches de Métallurgie Physique, CEA, Université Paris-Saclay, F-91191 Gif-sur-Yvette, France*

(Received 19 April 2019; revised manuscript received 11 September 2019; published 4 December 2019)

We study the magnetic short range order (MSRO) in $Fe_{1-x}Cr_x$ ($0 \leqslant x \leqslant 0.15$) where an inversion of atomic short range order (ASRO) occurs at $x_C = 0.11(1)$. Our combination of neutron diffuse scattering and bulk magnetization measurements offers a comprehensive description of these local orders at a microscopic level. In the dilute alloys ($x < 0.04$), the Cr atoms bear a large moment $\mu_{Cr} = -1.0(1)\ \mu_B$, antiparallel to the Fe ones (μ_{Fe}). They fully repel their Cr first and second neighbors, and perturb the surrounding Fe moments. With increasing x, near neighbor Cr-Cr pairs start to appear and the Cr moment magnitude decreases, while μ_{Fe} shows a rounded maximum for $x_1 = 0.06(1) < x_C$. Above x_C, ASRO turns to local Cr segregation, thereby increasing magnetic frustration. First-principles calculations reproduce the observed moment variations but overestimate the magnitude of the Cr moment. In order to reconcile theory with experiment quantitatively, we propose that the magnetic moments start canting locally, already above x_1. This picture actually anticipates the spin glasslike behavior of Cr-rich alloys. The whole study points out the subtle interplay of MSRO and ASRO, yielding an increasing frustration as x increases, due to competing Fe-Cr and Cr-Cr interactions and Cr clustering tendency.

DOI: 10.1103/PhysRevB.100.224406

I. INTRODUCTION

$Fe_{1-x}Cr_x$ alloys of concentration x between 0.02 and 0.2 are the main constituents of industrial ferritic steels, highly resistant to radiation damages and considered as leading candidates for use in future fusion reactors [1,2], since they minimize the effects of swelling, void formation, hardening, and atomic segregation induced by high energy neutron irradiation. In this concentration range, an inversion of atomic short range order (ASRO) occurs at $x_C = 0.11(1)$. Namely the Cr atoms repel each other below x_C, whereas they attract each other above x_C. For $x = x_C$ the atomic distribution is close to random. The mixing enthalpy changes sign [3–5] around x_C. This unique case in nature influences both the stability of the solid solutions and their resistance to irradiation. It was initially observed by neutron diffuse scattering and residual resistivity [6,7], then investigated by Mössbauer spectroscopy [8] and x-ray absorption fine structure (EXAFS) [9].

The origin of this surprising inversion comes from the peculiar band structure of FeCr ferromagnets, which controls both the atomic distribution and the microscopic magnetism. In metallic alloys it is known for a long time that the interactions between atoms, which govern their statistical distribution, can be written in terms of electronic pair potentials [10–12], although the total cohesive energy cannot [13]. In FeCr alloys, pioneering band structure calculations [14] performed in the coherent potential approximation (CPA) predicted the ASRO inversion before its experimental observation, and outlined the major role played by magnetism in this process. The physical picture derived from this approach is the following. Whereas pure Fe is a weak ferromagnet (the majority spin band is not completely full), pure Cr is a spin density wave antiferromagnet. Inserting Cr atoms in the Fe matrix lowers the local Cr density of state of the majority spin band at the Fermi level, due to the formation of a virtual bound state [15–17]. As a result, the Cr impurity couples antiferromagnetically to the Fe matrix with a strong magnetic moment, and the Cr atoms repel each other to screen the local magnetic perturbation. The pair potential between Cr near neighbors strongly varies with the filling of the d band. With an increase of the Cr concentration, it changes sign due the shift of the Fermi level with respect to the bound state, so that the Cr atoms with lower moments then tend to segregate.

Since the beginning of the century, due to the increasing interest in FeCr based steels for nuclear reactors, new calculations of the electronic band structure have been performed, using modern approaches and powerful computers. Atomistic simulations [18,19], first-principles theories [4,20–27], and tight-binding models [28–30] have been intensively developed. They investigated the changes in the Fermi surface topology, phase diagram, and cohesive properties (lattice constant, bulk modulus, enthalpy of formation) in great detail. They also calculated the chemical pair potentials [31] in excellent agreement with experiments, derived the effective magnetic interactions [26], and studied the effect of pressure [32]. Many approaches point out the crucial role of magnetic short range order (MSRO) in the cohesive and elastic properties [33], as well on the ASRO, diffusion coefficients, or decomposition kinetics [34] of $Fe_{1-x}Cr_x$ alloys.

Strikingly, with regards to this huge theoretical work, no direct measurement of the MSRO has been performed since

the 1970s. We focus here on the study of MSRO in $Fe_{1-x}Cr_x$ alloys ($0 \leqslant x \leqslant 0.15$) by neutron diffuse scattering, which yields direct information about magnetic moments and perturbations in binary alloys [35,36]. Namely, by combining bulk magnetization, polarized and unpolarized neutrons data, we obtain the average moments on Fe and Cr sites in absolute scale with their sign, and measure *quantitatively* how much a Cr moment modifies its neighbor moments in a dilute alloy. For this study we used samples previously measured [6,7] where the thermodynamic and ASRO state is well known. Knowing ASRO accurately, we deduce the MSRO from the nuclear-magnetic interference cross section of polarized neutrons [37,38]. It is directly related to the *algebraic* difference between Fe and Cr magnetic moments, and its modulations with the wave-vector transfer yield the magnetic moment distribution. Thanks to the polarized neutrons, increased neutron flux, and optimized experimental setup, we strongly improve the accuracy of this determination with respect to previous results [16,39–43]. We also fill the gap between these data, obtained either in dilute alloys ($x \sim 0.01$–0.02) [16,39–41] or in concentrated ones ($x \geqslant 0.15$) [42,43].

We compare quantitatively the local Fe and Cr moments and the magnetic perturbations with existing theories [4,14,25,44–46]. We also performed new first-principles calculations of the moments and perturbations taking into account the true ASRO of the samples. In $Fe_{1-x}Cr_x$ alloys, ASRO and MSRO are intrinsically correlated and interact in a subtle way as x increases. The concentration range studied here ($0 \leqslant x \leqslant 0.15$) where the ASRO inversion occurs is a nice playground to investigate such effects. It spans from the dilute case where the Cr induced changes of the band structure are crucial to the concentrated case where frustration plays a major role.

Magnetic frustration comes from the competition of Cr-Fe and Cr-Cr near neighbor interactions which start to coexist above the limit of full Cr-Cr repulsion ($x_R = 0.04$), and strongly increase above x_C when Cr atoms tend to segregate. The striking consequence of this frustration is a canting of the Cr moments, which starts to be observed between x_R and x_C, around $x_1 = 0.06(1)$. Taking this canting into account allows us to reconcile neutron data and first-principles calculations. Such canting is a natural precursor of the spin glass phases observed in Cr-rich alloys ($x \sim 0.8$). The whole study provides a comprehensive picture of the ASRO and MSRO interplay in $Fe_{1-x}Cr_x$ alloys.

II. EXPERIMENTS

A. Sample synthesis and experimental details

Polycrystalline samples were synthesized by CECM-Vitry, Cristaltech Grenoble, Gero-Neuhausen, and Ceracmilwaukee, with concentrations in the range $0 \leqslant x \leqslant 0.15$. Bulk cylinders of 30-mm length and 9-mm diameter were carved from the synthesized materials for the neutron experiments. The samples homogeneity and the Cr concentrations were checked by chemical analysis. In the Fe-Cr system, the phase diagram shows a miscibility gap [47,48] so that with increasing x, the solid solution starts to decompose into two body centered cubic (bcc) phases, enriched in Fe and Cr, respectively. The solubility limit of Cr in Fe is estimated to $x = 0.11$ at 793 K and $x = 0.07$ at 703 K. Although such decomposition may occur here in principle, its kinetics is much slower than the ASRO kinetics. The latter was precisely determined by measuring the residual resistivity [6,49,50], yielding the suitable heat treatment [7].

After an homogenization at 800 °C, the samples were heated in a quartz tube at 520 °C, a temperature where ASRO at equilibrium is immediately reached. Then the temperature T was gradually decreased down to 430 °C. The samples were kept at 430 °C for 10 h and quenched into water, so that the ASRO measured afterwards corresponds to thermal equilibrium at 430 °C. In such a condition, precipitation does not occur and the solid solution remains homogeneous in all samples. For the highest concentration $x = 0.15$ close to the miscibility gap, ASRO at 430 °C evolves with the annealing time. This evolution is a precursor of segregation, expected in thermally aged concentrated samples at timescales exceeding 10^4 h [51]. To check its influence on the magnetic order, we measured two alloys with $x = 0.15$, one annealed at 430 °C during 10 h (as for all other samples) and one annealed during 84 h before quenching.

Neutron measurements were performed on the G6.1 diffractometer of the Orphée reactor in Saclay, equipped with a multidetector and a focusing graphite monochromator, with an incident neutron wavelength of 4.73 Å.

The range of the scattering vector ($0.1 \leqslant K \leqslant 2.5$ Å^{-1}) avoids any parasitic contribution from the Bragg scattering. The measurements were performed at low temperature (8 K) using a cryogenerator, which suppressed almost completely the contributions from magnetic or lattice excitations to the diffuse scattering, considered as purely elastic in the following. A vertical magnetic field of 1.5 T provided by an electromagnet saturated the sample in the direction perpendicular to the scattering plane ($\mathbf{K} \perp \mathbf{H}$). The bulk sample cylinders were directly screwed to the cold head, without a sample holder, and oriented with their axis along the magnetic field. This geometry minimizes the demagnetization field. In the heat treated bulk samples, there is no preferential orientation of the grains when the magnetic field is applied. An electromagnet and cryogenerator were placed inside a vacuum chamber which strongly decreased the environmental background. To determine the neutron cross sections in absolute scale, the intensities were corrected for background, absorption [52,53], and multiple scattering [54], and calibrated by measuring vanadium and cadmium standards carved with the same shape and volume as the samples, as well as the empty equipment. Due to the large incident neutron wavelength, no Bragg peaks are seen from the sample which simplifies the corrections. These corrections are detailed in the Supplemental Material [55].

Unpolarized neutron measurements performed in the saturating field were combined with measurements in zero magnetic field to separate the nuclear and magnetic cross sections [56,57]. Polarized neutron measurements were performed with the saturating field and the same experimental conditions, with the incident neutron polarization along the magnetic field. We used either a Cu_2MnAl Heussler alloy or a FeCo supermirror to polarize the incident neutron beam. Reversal of the neutron spin polarization was achieved by a Mezei-type flipper. The incident polarization ($P = 0.98$) and

the flipping efficiency ($e = 0.99$) were taken into account to determine the interference nuclear-magnetic cross sections.

Polished spheres of about 2 mg were made out of the neutron samples to measure the magnetization. Their static magnetization was measured at 5 K up to a field $H = 6$ T using a superconducting quantum interference device (SQUID) magnetometer and corrected for demagnetization effects. The magnetization of a pure iron sample was measured for calibration.

B. Atomic and magnetic short range order as measured by neutron diffuse scattering

The general expression of the neutron cross section [57] includes nuclear and magnetic scattering. A nuclear-magnetic interference term adds when the incident neutron beam is polarized. Here we only consider elastic scattering, without change of the neutron energy. The nuclear scattering by independent nuclei of scattering length b_i involves an incoherent (K-independent) term proportional to $\overline{b^2} - \bar{b}^2$, reflecting the distribution of isotopes and nuclear moments. In a random binary alloy, an elastic nuclear diffuse (Laue) scattering, coming from substitution disorder, adds to the incoherent scattering. ASRO gives rise to modulations of the average Laue contrast, $\Delta b = b_{\mathrm{Cr}} - b_{\mathrm{Fe}}$ for a FeCr alloy, where $b_{\mathrm{Cr}} = 0.3635(7) \times 10^{-12}$ cm and $b_{\mathrm{Fe}} = 0.945(2) \times 10^{-12}$ cm are the coherent scattering lengths of Cr and Fe atoms, respectively.

The magnetic scattering results from the neutron interaction with unpaired electrons. In a binary ferromagnetic (FM) alloy with a given ASRO, it arises from the distribution of magnetic moments, namely here from different Cr and Fe moments (μ_{Cr} and μ_{Fe}, respectively), which depend on their local environment. The MSRO parameters yield modulations of the average magnetic contrast ($\Delta\mu = \mu_{\mathrm{Cr}} - \mu_{\mathrm{Fe}}$). Owing to selection rules, only the moment components being perpendicular to **K** contribute to the magnetic scattering. In a FM alloy, this feature can be used to separate the nuclear and magnetic cross sections, by using different orientations of the magnetic field.

Under a magnetic saturating field **H** perpendicular to the scattering vector **K**, the diffuse scattering of polarized neutrons from a FM alloy is the sum of three contributions:

$$\frac{d\sigma}{d\Omega} = \left(\frac{d\sigma}{d\Omega}\right)_N + \left(\frac{d\sigma}{d\Omega}\right)_M + \epsilon\left(\frac{d\sigma}{d\Omega}\right)_{NM}, \tag{1}$$

where the subscripts N, M, and NM refer to the the nuclear, magnetic, and interference nuclear-magnetic cross sections, respectively [56,57]. These terms are, respectively, proportional to the Fourier transforms of the atomic correlations between neighbor sites, spin correlations between neighbor moments, and site-moment correlations [38]. The neutron polarization ϵ is either parallel ($\epsilon = 1$) or antiparallel ($\epsilon = -1$) to the magnetic field. The interference term is extracted by measuring cross sections for the two neutron spin states and taking their difference.

For unpolarized neutrons ($\epsilon = 0$), the interference term cancels and the nuclear and magnetic cross sections can be extracted by measuring the cross sections in two configurations, namely in zero field when magnetic domains are randomly oriented:

$$\left(\frac{d\sigma}{d\Omega}\right)_{H=0} = \left(\frac{d\sigma}{d\Omega}\right)_N + \frac{2}{3}\left(\frac{d\sigma}{d\Omega}\right)_M, \tag{2}$$

and under a saturating field **H** aligning the domains in the direction perpendicular to the scattering vector **K**:

$$\left(\frac{d\sigma}{d\Omega}\right)_{\mathbf{H}\perp\mathbf{K}} = \left(\frac{d\sigma}{d\Omega}\right)_N + \left(\frac{d\sigma}{d\Omega}\right)_M. \tag{3}$$

Following the model of Cowley-Warren [58], the nuclear cross section is expressed as

$$\left(\frac{d\sigma}{d\Omega}\right)_N = \left(\frac{d\sigma}{d\Omega}\right)_{\mathrm{inc}} + x(1-x)(b_{\mathrm{Cr}} - b_{\mathrm{Fe}})^2\, S(\mathbf{K}), \tag{4}$$

where the first term is the incoherent nuclear scattering cross section, defined as

$$\left(\frac{d\sigma}{d\Omega}\right)_{\mathrm{inc}} = \frac{1}{4\pi}\left[(1-x)\sigma_{\mathrm{inc}}^{\mathrm{Fe}} + x\sigma_{\mathrm{inc}}^{\mathrm{Cr}}\right], \tag{5}$$

with $\sigma_{\mathrm{inc}}^{\mathrm{Fe}} = 0.400$ barn and $\sigma_{\mathrm{inc}}^{\mathrm{Cr}} = 1.83$ barn. The second term of Eq. (4) is the Laue scattering, modulated by the ASRO function $S(\mathbf{K})$.

$S(\mathbf{K})$ is expressed in terms of the ASRO parameters α_i. For a binary alloy $A_{1-x}B_x$, they are defined as

$$\alpha_i^{AB} = 1 - \left(\frac{n_i^A}{c_A\, z_i}\right). \tag{6}$$

In Eq. (6), n_i^A is the number of A atoms on the ith neighbor shell of a B atom placed at the origin, $c_A = 1 - x$ is the concentration of A atoms, and z_i is the coordination number of the ith shell. Noticing that $\alpha_i^{AB} = \alpha_i^{BA}$, the ASRO parameters are simply quoted α_i in the following. A positive (negative) α_i value corresponds to an attractive (repulsive) order between the central atom and atoms of the same type in ith shell. The values $\alpha_i = 0$ and $\alpha_i = -x/(1-x)$ correspond to random distribution and full atomic repulsion in the ith shell, respectively. When averaged for a polycrystalline sample over all **K** orientations, the ASRO function $S(K)$ writes

$$S(K) = 1 + \sum_i z_i\, \alpha_i\, \frac{\sin KR_i}{KR_i}, \tag{7}$$

where R_i is the radius of the ith shell.

If the magnetic moments are collinear, the magnetic moment distribution reduces to a one-dimensional case. In such a case, an expression of the magnetic cross section was derived by Marshall [35,57] and Gautier [36] assuming that (i) the magnetic perturbations add linearly, (ii) the two constituents have the same isotropic magnetic form factor $F(K)$, and (iii) the ASRO can be treated as a perturbation to the case of a random alloy. The nuclear-magnetic interference term was calculated by Medina and Cable [37,38] under the same assumptions. The magnetic and nuclear-magnetic cross sections expressed in mbarn sr^{-1} at^{-1} write

$$\left(\frac{d\sigma}{d\Omega}\right)_M = \left(\frac{\gamma e^2}{2m_e c^2}\right)^2 x(1-x)\, S(\mathbf{K})\, F(K)^2\, T(\mathbf{K}) \tag{8}$$

and

$$\left(\frac{d\sigma}{d\Omega}\right)_{NM} = \left(\frac{\gamma e^2}{m_e c^2}\right) x(1-x)(b_{\mathrm{Cr}} - b_{\mathrm{Fe}}) S(\mathbf{K})\, F(K)\, M(\mathbf{K}), \tag{9}$$

where γ is the neutron gyromagnetic ratio and $\frac{\gamma e^2}{2m_e c^2} = 0.2695 \times 10^{-12}$ cm μ_{B}^{-1}.

The MSRO function $M(\mathbf{K})$ writes

$$M(\mathbf{K}) = \mu_{\mathrm{Cr}} - \mu_{\mathrm{Fe}} + (1-x)\, G(\mathbf{K}) + x\, H(\mathbf{K}) + W(\mathbf{K}), \tag{10}$$

where $G(\mathbf{K})$ [$H(\mathbf{K})$] is the Fourier transform of the perturbation $g(\mathbf{R})$ [$h(\mathbf{R})$] produced by a Cr moment at a vector $\mathbf{R}$ of a Fe (Cr) moment. $W(\mathbf{K})$ is a corrective term due to ASRO. If the perturbations add linearly, the correlation functions verify the relation

$$T(\mathbf{K}) = M(\mathbf{K})^2. \tag{11}$$

For a polycrystalline sample, simplified expressions of the magnetic cross sections can be obtained by replacing in Eqs. (8)–(11), the ASRO and MSRO functions by their spherical averages:

$$M(K) = \mu_{\mathrm{Cr}} - \mu_{\mathrm{Fe}} + w_0 + \sum_i z_i\, \phi_i \frac{\sin KR_i}{KR_i}. \tag{12}$$

The MSRO parameters ϕ_i combine the perturbations $g_i = g(R_i)$ induced by a Cr moment on its neighboring Fe moments and the perturbations $h_i = h(R_i)$ on its neighboring Cr moments as

$$\phi_i = (1-x)\, g_i + x\, h_i + w_i, \tag{13}$$

where the corrective terms w_i can be expressed as

$$w_i = (1-2x)\, \alpha_i\, (h_i - g_i). \tag{14}$$

The average magnetization $\overline{\mu}$ of the sample writes

$$\overline{\mu} = (1-x)\, \mu_{\mathrm{Fe}} + x\, \mu_{\mathrm{Cr}}. \tag{15}$$

The term $w_0 = \sum_i z_i w_i$ in Eq. (12) is a small correction to the moment difference [36]. Notice that μ_{Cr}, μ_{Fe}, and the magnetic perturbations depend on concentration and amount of ASRO. At very low x values, we can identify the ϕ_i parameters with the perturbations g_i of the Fe moments. In the simple case of a random alloy [$S(K) = 1$] without magnetic perturbations ($\phi_i = 0, \forall i$), the MSRO function $M(K)$ reduces to the algebraic difference $\Delta\mu = \mu_{\mathrm{Cr}} - \mu_{\mathrm{Fe}}$ and the magnetic cross section varies like the squared magnetic form factor $F(K)^2$. Any departure from this variation is a direct evidence of ASRO or MSRO.

The average MSRO function $\langle M(K) \rangle$ measures the magnetic contrast $\Delta\mu$, analogous to the Laue contrast Δb. $\Delta\mu$ is obtained whatever the microscopic description of the ASRO and MSRO, under the only assumption of a collinear medium. Although collinearity is widely observed in Fe-based alloys, a careful analysis of the data and close comparison with theory suggest that it does not hold for FeCr alloys, even at low Cr content. This led us to propose a correction to the above models, as discussed in Sec. IV B and the Supplemental Material [55]. We show that spin canting induces a small but measurable contribution to the incoherent neutron cross section, which is indeed observed experimentally and represents a key result of our study.

C. Neutron results

The nuclear, magnetic, and nuclear-magnetic cross sections are shown for selected samples in Fig. 1. They all show strong modulations with K. The inversion of ASRO is clearly seen on the nuclear cross section: below x_C the intensity shows a broad maximum with K and decreases in the low K range due to atomic repulsion between neighbor Cr pairs, whereas above x_C it increases monotonously at low K values, showing that the Cr atoms tend to segregate, although the studied alloys never host actual clusters.

To analyze the magnetic terms, we treat the ASRO and MSRO in the same way, by restricting the number of SRO parameters to the five first neighbor shells and grouping them for close concentric shells [7]. This procedure is imposed by the limited K range of measurement and justified for a bcc alloy where the shells 1 and 2 ($R/a = 0.866$ and 1, where a is the lattice constant) and 4 and 5 ($R/a = 1.66$ and 1.73), are close to each other.

We first fit the nuclear cross section to determine ASRO parameters entering in the function $S(K)$, as in Ref. [7]. The averaged ASRO parameter corresponding to the grouped (i, j) shell of coordination $z_i + z_j$ and radius $R_{ij} = (z_i R_i + z_j R_j)/(z_i + z_j)$ is defined as $\alpha_{ij} = (z_i \alpha_i + z_j \alpha_j)/(z_i + z_j)$, namely $\alpha_{12} = (8\alpha_1 + 6\alpha_2)/14$ and $\alpha_{45} = (24\alpha_4 + 8\alpha_5)/32$.

In a second step, we fix the ASRO parameters to determine the magnetic functions $M(K)$ and $T(K)$ using Eqs. (8) and (9). The magnetic form factor $F(K)$ is taken as the form factor of pure iron and approximated by the formula $F(K) = \exp(-0.061K^2)$ which is valid in the experimental K range [59]. As shown in Fig. 2(a), $M(K)$ shows strong modulations due to the MSRO parameters, but Eq. (11) which relates $M(K)$ and $T(K)$ obtained from different experimental configurations is well obeyed within the experimental accuracy [Fig. 2(b)]. This means that although being strong, the magnetic disturbances induced by a Cr moment on its Fe and Cr neighbors add linearly, being mostly limited to the first five neighbor shells.

The MSRO parameters averaged over the 1 and 2 and 4 and 5 shells are defined as $\phi_{12} = (8\phi_1 + 6\phi_2)/14$ and $\phi_{45} = (24\phi_4 + 8\phi_5)/32$, as for the ASRO parameters. They were mostly determined from the polarized neutron data and the function $M(K)$ [using Eq. (12)] since the accuracy is much higher. By limiting the parameters to five neighbors, we obtain a good fit of $M(K)$ for all concentrations. The fitted MSRO parameters $\Delta\mu$, ϕ_{12}, ϕ_3, and ϕ_{45} are plotted as a function of Cr concentration x in Fig. 3. The error bars include both the fit error bar and the dispersion of results when the number of shells included in the fit is varied between 5 and 8. $\Delta\mu$ and ϕ_{12} are determined with the best accuracy and stability.

The average moments on the Cr and Fe sites were determined by combining the neutron results (yielding $\Delta\mu = \mu_{\mathrm{Cr}} - \mu_{\mathrm{Fe}}$) to the magnetization data [Eq. (15)]. We took an error bar of about 1% for the absolute calibration of the

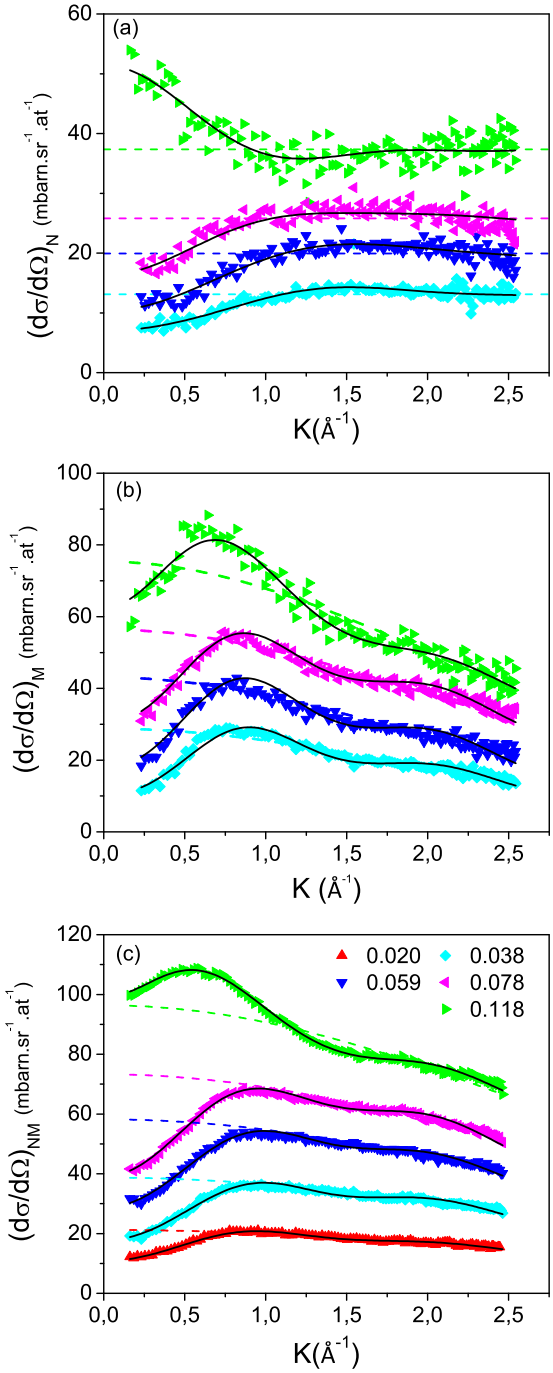

FIG. 1. Neutron diffuse cross section of $Fe_{1-x}Cr_x$ alloys. (a) Nuclear cross section (corrected for incoherent scattering). (b) Magnetic cross section. The curves for $x = 0.078$ and 0.118 are shifted by 10 mbarns sr^{-1} at^{-1} for clarity. (c) Nuclear-magnetic cross section deduced from polarized neutron scattering. Colors and symbols are the same for the three panels. Solid lines are fits of Eqs. (8)–(11) to the data, involving ASRO and MSRO parameters up to the fifth shell (see text). Dashed lines show the variation expected in the absence of ASRO or MSRO.

magnetization. Our magnetization data compare well with those of Aldred [60], performed on samples quenched from 825 °C. A small effect of the ASRO on the magnetization is observed (see the Supplemental Material [55] for details).

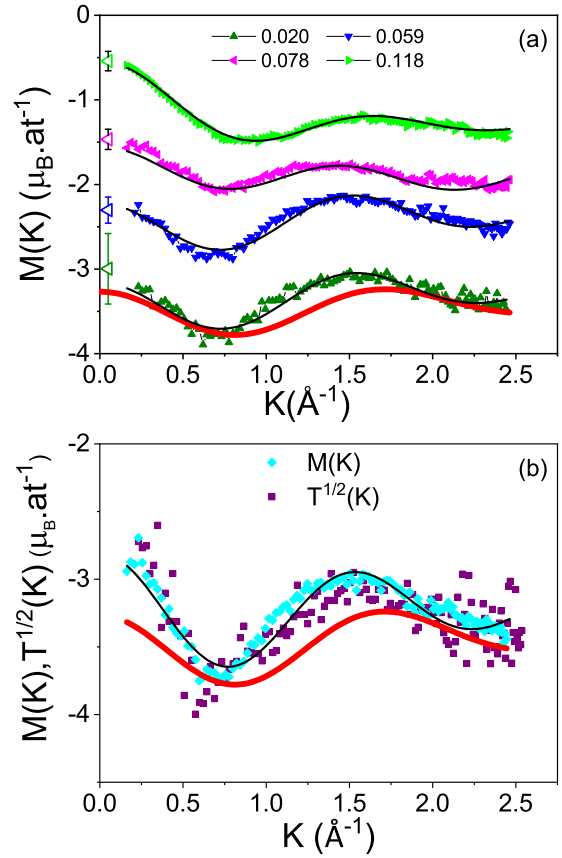

FIG. 2. (a) Magnetic function $M(K)$ for selected $Fe_{1-x}Cr_x$ samples. For clarity, the curves are shifted by 0.8 μ_B (1.2 and 1.6 μ_B) for $x = 0.058$ (0.078 and 0.118). Solid lines are fits up to ϕ_{45}. Large empty triangles are extrapolations at $K = 0$ deduced from bulk magnetization. (b) Comparison between $M(K)$ and $T(K)^{0.5}$ for $x = 0.038$. Thick red lines are calculation with $\phi_i = g_i$, made by Drittler [46] for $x \sim 0$.

For $x = 0.15$, where the ASRO strongly varies with the heat treatment, we also observe a small effect of the ASRO on the magnetization. The ASRO increases with decreasing the annealing temperature or increasing the annealing time, as shown by the strong increase of the nuclear cross section at low K values [Fig. 4(a)]. This tendency can be monitored by the value $S(0)$ of the fitted ASRO function $S(K)$ for $K = 0$. Concomitantly, the magnetic cross section increases at low K [Fig. 4(b)], the magnetization shows a small increase [Fig. 4(c)], and the magnitude of the Cr moment decreases from 0.8 to 0.2 μ_B [Fig. 4(d)].

As expected from the ASRO inversion, chosen concentration range, and heat treatment, we do not observe segregation in any of the studied alloys. For $0.2 < x < 0.4$, such segregation can be detected by neutron small angle scattering [61,62], atom probe tomography [51], and its kinetics simulated by atomistic Monte Carlo [63] and dynamic [64] simulations. In the nuclear cross section, it would appear as an intensity peak in the range $0.1 \leqslant K \leqslant 0.4$ Å^{-1} related to the typical distance between precipitates [65]. Such signal is indeed absent from our neutron patterns. For $x = 0.15$, a sample on the border of the miscibility gap, the evolution of the ASRO with annealing time is a precursor of segregation. True segregation may occur

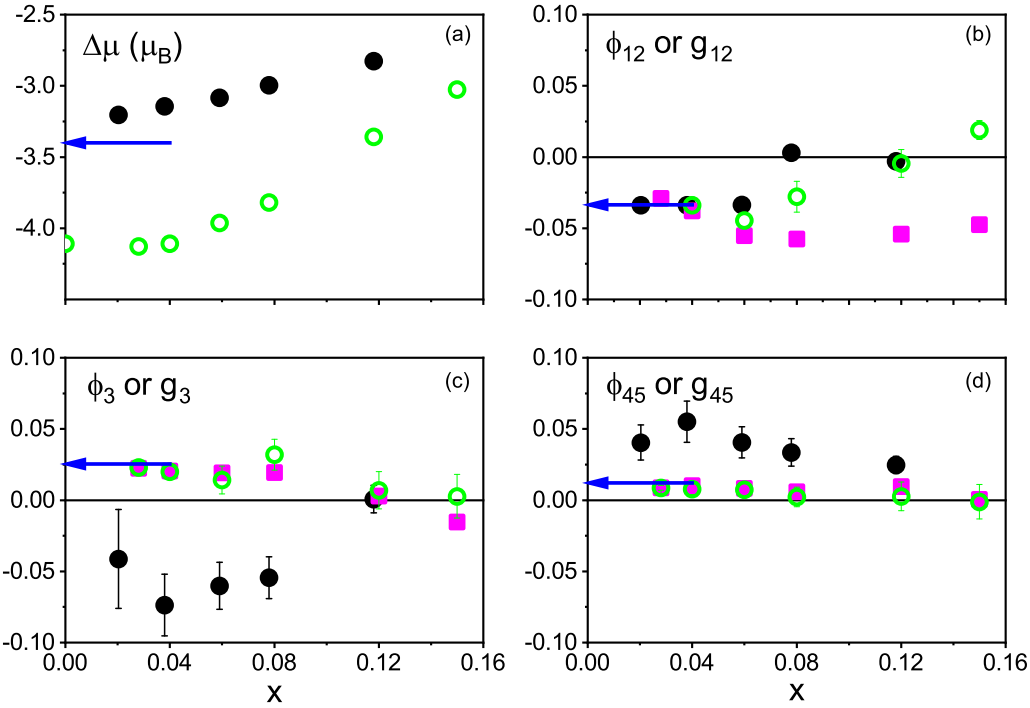

FIG. 3. MSRO parameters in $Fe_{1-x}Cr_x$ alloys versus x. (a) $\Delta\mu = \mu_{Cr} - \mu_{Fe}$ and perturbations (b) ϕ_{12}, (c) ϕ_3, and (d) ϕ_{45} induced by a Cr moment on its five first neighbor shells. The experimental determinations (black dots) are compared to first-principles calculations (open green dots). The calculated perturbations g_{12}, g_3, and g_{45} on the Fe neighbors are also plotted (magenta squares). Arrows indicate the first-principles predictions of Drittler *et al.* [46] in the dilute impurity limit.

in such samples at much longer thermal aging times, or if Cr precipitation is accelerated under irradiation [66–68].

In all our samples we only observe fluctuations of concentrations at the atomic scale. However, the Cr moment is strongly sensitive to its local environment, an effect which is well reproduced by first-principles calculations, as shown below.

III. FIRST-PRINCIPLES CALCULATIONS

First-principle calculations were performed to calculate the magnetic moment distribution (Fe and Cr moments, MSRO parameters) in simulated alloys having the same atomic distribution as the studied alloys, namely the same ASRO parameters. They thus provide a direct comparison between experiment and theory (Sec. IV).

A. Density functional theory (DFT) method

We used the density functional theory (DFT) with the projector augmented wave (PAW) method [69,70] as implemented in the VASP (Vienna *ab initio* simulation package) code [71–73]. Calculations were performed using either the generalized gradient approximation (GGA) for the exchange-correlation functional in the Perdew-Burke-Ernzerhof (PBE) form [74], or the local density approximation (LDA). LDA calculations were performed adopting the same GGA optimized lattice parameters (2.830 to 2.836 Å from the smallest to the largest Cr concentration). We recall that GGA predicts correctly the ground state of Fe, being the FM bcc phase, while LDA does not. All the calculations are spin polarized and within the collinear magnetism approximation. $3d$ and $4s$ electrons of Fe and Cr atoms were considered as valence electrons. The plane-wave basis cutoff was set to 400 eV. The convergence cutoff for the electronic self-consistency loop was set to $\Delta E = 10^{-6}$ eV. Atomic magnetic moments are obtained by a charge and spin projection onto the PAW spheres [72,73] as defined by the adopted PAW potentials. The corresponding radius for Fe and Cr atoms are 1.30 and 1.32 Å, respectively. We have estimated the dependence of the local moments on the chosen criterion. The change of Fe (Cr) moment is at most 1% (4%) if using either the present criterion or a 10% variation of the sphere radius with respect to the half interatomic distance. Fe and Cr moments can also be sensitive to the lattice constant. The lattice constant of bcc $Fe_{1-x}Cr_x$ alloys at RT varies from 2.865 ($x = 0$) to 2.873 Å ($x = 0.15$) [75]. We have verified that the Fe (Cr) moments increase up to 2% (9%) when the lattice constant increases from the GGA value at zero temperature (2.83 Å) to the experimental value of iron (2.86 Å).

The calculations show that the local moments on Fe and Cr sites strongly depend on their local environment. This is shown in the Supplemental Material [55] where the Fe (Cr) moments are plotted versus the number of their Cr neighbors in the first two shells. Both Fe and Cr moments decrease in absolute value when Cr atoms are located in their first two neighbor shells.

Calculations were performed to simulate dilute $Fe_{1-x}Cr_x$ alloys with as close as possible ASRO as the experimental samples, using supercells of $5 \times 5 \times 5$ times the lattice parameter of the cubic unit cell (a_0), containing 250 bcc atom sites each. All the atomic positions, the volume, and the

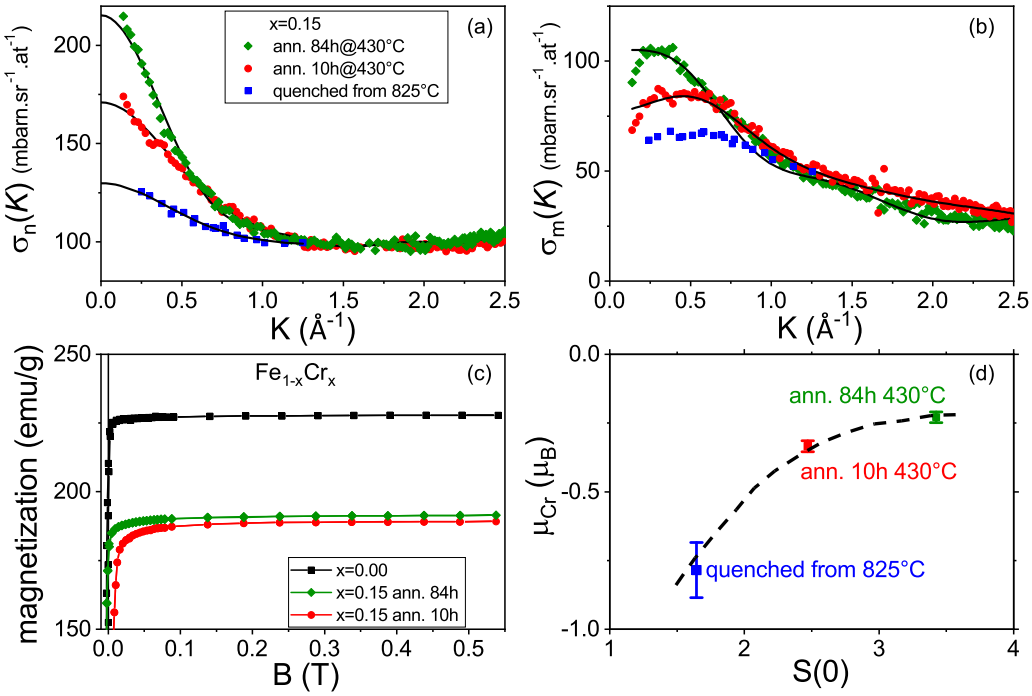

FIG. 4. Influence of the ASRO on the Cr moment and bulk magnetization of $Fe_{1-x}Cr_x$ alloys with $x = 0.15$. ASRO can be monitored by the heat treatment. Nuclear (a) and magnetic (b) cross sections measured for three samples with different heat treatments: quenched from 825 °C (from Aldred *et al* [43], blue squares), annealed at 430 °C for 10 h as for the whole series of samples (sample S1, red bullets), annealed at 430 °C for 84 h (sample S2, green diamonds). Solid lines are fits with 8 ASRO parameters in (a) and 5 MSRO parameters in (b). (c) Magnetization versus the internal magnetic field B at 5 K for S1, S2, and an iron sample. (d) Influence of the clustering tendency on the Cr moment: μ_{Cr} is plotted versus the value $S(0)$ of the ASRO function $S(K)$ at $K = 0$, as determined from the fits in (a).

shape of the supercells are fully optimized. The maximum residual force and stress are, respectively, 0.02 eV/A and 1.0 kbar. The k-point grids used in our calculations were chosen to achieve a k-sampling equivalent to a bcc cubic unit cell with a $15 \times 15 \times 15$ grid, following the Monkhorst-Pack scheme [76]. The Methfessel-Paxton broadening scheme with 0.1 eV width was applied [77]. We checked that the magnetic configurations are well converged with respect to the choice of k-point grids and the cutoff conditions.

B. Generation of atomic configurations with a given chemical SRO

In order to construct supercells with ASRO parameters close to those of the studied samples, we generated, for each studied Cr concentration, 100 000 atomic configurations with Fe and Cr atoms randomly distributed in the 250-site supercells and calculated the average SRO parameters $\overline{\alpha_i^{AB}}$ and the standard deviation of SRO parameters $\sigma(\alpha_i^{AB})$ in each case. Usually, many generated systems have the same set of SROs, with $\overline{\alpha_i^{AB}}$ close to the given experimental value. Among those, the system with the smallest deviation $\sigma(\alpha_i^{AB})$ was chosen. For the two lowest Cr concentrations (2.8% and 4% Cr), we have considered three supercells for each case, in order to improve the statistics of the properties of our interest, in particular the local magnetic moment on each atom. Table I gives a comparison of SRO parameters between the calculation on supercells and the experiments. For each alloy concentration, average Fe and Cr moments are obtained for a comparison with experimental data. The standard deviation of the calculated moments is around 0.03 μ_B for each case.

C. Results

The g_i, h_i, and w_i parameters were calculated for each concentration (see the Supplemental Material [55] for details). Using Eqs. (13) and (14), one deduces the perturbations ϕ_i. In Fig. 5 the magnetic perturbations g_{12}, h_{12}, w_{12}, and ϕ_{12} averaged on the first two shells are shown versus x. The

TABLE I. ASRO parameters α_{12} and α_3 deduced from experiments (neutron data) and DFT simulations. The three samples with $x \sim 0.15$ have received different heat treatments; $x = 0.1523$: annealed at 430 °C during 10 h and quenched; $x = 0.1506$: annealed at 430 °C during 3.5 days and quenched; $x = 0.15$: quenched from 825 °C.

Experiment			Simulation		
x	α_{12}	α_3	x	α_{12}	α_3
0.028	−0.032(2)	−0.012(7)	0.028	−0.0288	−0.0043
0.038	−0.028(2)	−0.012(6)	0.04	−0.0268	−0.0069
0.059	−0.028(3)	−0.014(14)	0.06	−0.0233	0.0071
0.078	−0.015(3)	−0.019(16)	0.08	−0.0171	−0.0054
0.118	0.010(3)	0.021(13)	0.12	0.0097	0.0152
0.1523	0.063(4)	0.010(35)	0.152	0.0602	0.0070
0.1506	0.067(14)	0.003(6)	0.152	0.0646	0.0070
0.15	0.025(3)	−0.042(6)	0.152	0.0247	−0.0086

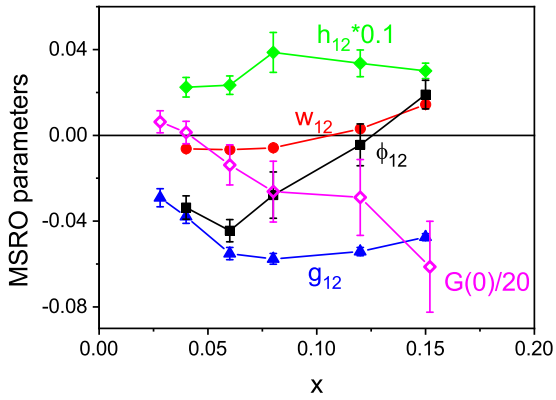

FIG. 5. $Fe_{1-x}Cr_x$ alloys. Magnetic perturbations calculated by DFT versus x, averaged for the first two neighbor shells: g_{12} (blue triangles), h_{12} (green diamonds), w_{12} (red bullets), and ϕ_{12} (black squares). The error bars on h_{12} are large because of the small number of Cr atoms. At $x = 0.028$, due to the absence of first and second neighbor Cr-Cr pairs, h_{12} could not be calculated. In the figure, h_{12} has been divided by 10. The total perturbation $G(0)$ divided by 20 is also plotted (magenta lozenges).

perturbation h_{12} on Cr atoms is about ten times larger than the perturbation g_{12} on the Fe atoms. The correction w_{12} due to ASRO is small. The weighted perturbation ϕ_{12} is negative, but decreases in amplitude for the highest concentrations due to the effect of h_{12}. The total perturbation $G(0) = \sum_i z_i g_i$, induced by a Cr moment on its Fe neighbors up to the fifth shell, changes sign and becomes negative for $x \sim 0.06$.

The summarizing Fig. 6 reports the concentration dependence of the Cr and Fe moments, and of the average magnetization. Figures 6(b) and 6(c) include the calculations of the previous section, as well as previous calculations and experimental data. The calculated perturbations ϕ_i are also readily compared to the experimental MSRO parameters (Fig. 3). The whole results are discussed in the next section.

IV. DISCUSSION

By combining polarized and unpolarized neutrons, we have experimentally determined the average moments on Fe and Cr sites, taking ASRO and MSRO into account. Polarized neutrons data yield the magnetic contrast $\Delta\mu$ with its sign, therefore determine the sign of the Cr moment unambiguously. μ_{Cr} is negative, namely antiparallel to the μ_{Fe}, and locally perturbs its neighbors up to the fifth neighbor shell.

When comparing the experimental Cr and Fe moments with their calculated counterparts, one could first of all wonder about the meaning of the local moment produced in each case. In the neutron scattering experiments, μ_{Cr} and μ_{Fe} are deduced from an integration of the unpaired electron density over the Wigner-Seitz (WS) cell of the atoms, or equivalently the first Brillouin zone in reciprocal space. In the DFT calculation, the WS cell is replaced by a sphere having the appropriate number of electrons. This could introduce a small difference between the two quantities (typically 0.1 μ_B) due to the presence of a small negative electron density on the border of the WS cell. As discussed below, such effect cannot explain the large difference (up to a factor 2) between experiment and theory.

In the following, we discuss the experimental results (moments and perturbations) in comparison with the calculated values obtained in Sec. III and in the literature. We consider the dilute impurity limit and the concentrated alloys successively. We suggest that Cr moment *cant* when the Cr concentration exceeds a critical concentration ($x_1 \sim 0.06$), below the concentration of inversion [$x_C = 0.11(1)$]. Taking this canting into account, one can reconcile experiment and theory in a large extend.

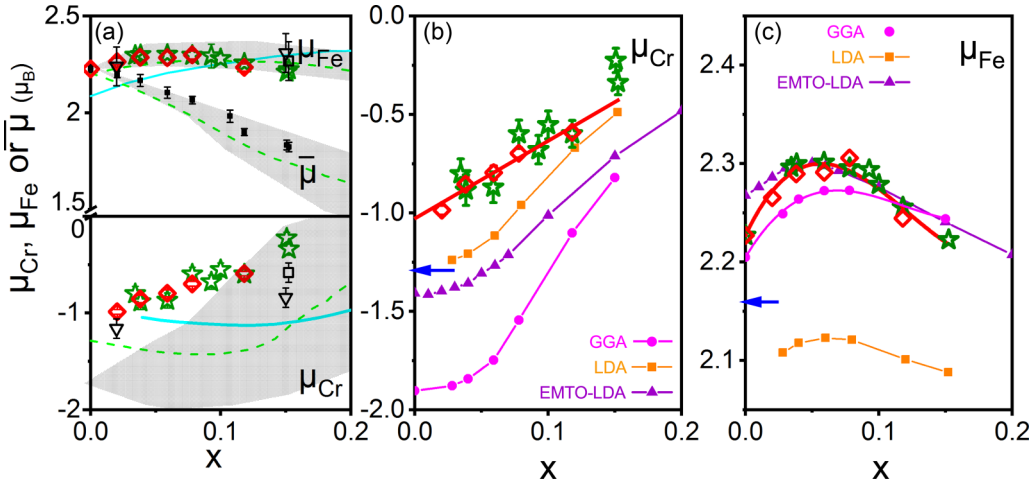

FIG. 6. $Fe_{1-x}Cr_x$ alloys. Variation of the magnetic moments μ_{Cr} and μ_{Fe} and average magnetization $\overline{\mu}$ with the Cr concentration x, in comparison with previous results and calculations. (b) and (c) Zooms of (a). Experiment: Present data: polarized neutrons (red open lozenges), unpolarized neutrons (green stars), magnetization (full black squares). Data from Shull [39] (open triangles) and Aldred [43] (open squares). The error bars on μ_{Fe} (typically 0.05 μ_B for our data and 0.10 μ_B for previous results) are not shown for clarity. Calculations: TB from Hennion [14] (dashed green lines); Sacchetti [45] (solid turquoise blue lines); LDA-KKR from Drittler [46] (dark blue arrows); GGA from Klaver[4] (shaded regions); EMTO-LDA from Ruban [25] (purple triangles); GGA, this work (magenta bullets); LDA, this work (orange squares); solid lines in (b) and (c) are guides for the eye.

A. Dilute impurity limit

In the dilute impurity limit ($x < 0.01$), our neutron data extrapolate to a negative moment $\mu_{Cr} = -1.0(1)\ \mu_B$ antiparallel to that of the Fe matrix. This large negative moment is induced by the creation of a virtual bound state in the majority spin band. As shown in Fig. 6, all calculations predict the correct sign, but they systematically overestimate the magnitude $|\mu_{Cr}|$. Moreover, the predicted μ_{Cr} strongly depends on the theoretical methods and approximations employed, particularly on the exchange-correlation functional. In the dilute limit, our LDA-predicted moment ($\mu_{Cr} = -1.3\ \mu_B$) is closer to experiment than our GGA-predicted one ($-1.9\ \mu_B$), which situates quite far from the experimental data. Previous GGA calculations [4,29] yield μ_{Cr} between -1.5 and $-1.8\ \mu_B$. Drittler *et al.* [46], using the Korringa-Kohn-Rostocker LDA-KKR approach, obtained $\mu_{Cr} = -1.3\ \mu_B$ as in our LDA results. More recently, Ruban *et al.* [25] performed LDA calculations by means of the exact-muffin-tin-orbital (EMTO) method in the coherent potential approximation (CPA). They adopted a lattice parameter of 2.87 Å and obtained $\mu_{Cr} = -1.4\ \mu_B$. Besides these first-principles calculations, Hennion [14] predicted quite reasonably the Cr moments using a tight-binding (TB) approach, whereas Sacchetti *et al.* [44,45] reported a too weak $\mu_{Cr}(x)$ variation.

The values of μ_{Fe} predicted for the Fe matrix are much closer to the experimental one, with small shifts [Fig. 6(c)]. To make a quantitative comparison, we recall here that the neutron experiments measure both spin and orbital contributions, whereas in all DFT calculations the orbital magnetic moment is neglected. The Fe orbital moment can be estimated to about 0.06 to 0.08 μ_B from experiment [78] and theory [79]. So the experimental value of 2.23 μ_B corresponds to a spin Fe moment of about 2.16 μ_B. Our GGA and LDA results (2.20 and 2.10 μ_B, respectively) sit on each side of this spin value, and close approximations are obtained using EMTO-LDA (2.26 μ_B) [25] and LDA-KKR (2.15 μ_B) [46].

In the dilute limit, the contributions of the perturbations h_i to $M(K)$ can be neglected [Eq. (13)] and the MSRO parameters ϕ_i reflect the perturbations g_i on the Fe neighbors of a Cr impurity. As found experimentally from the fitted ϕ_i parameters, a Cr atom decreases the moments of its first/second Fe neighbors by about 5% and it increases the moments of the fourth/fifth Fe neighbors by about the same amount (Fig. 3). As a general result, the perturbation parameters ϕ_i calculated by GGA or LDA up to the fifth shell well agree with the experimental ones. They have the right amplitude and the correct sign, besides ϕ_3 where the experimental value shows a large error bar. The shape of the calculated [46] magnetic function $M(K)$ also compares well with the experimental one for the dilute alloys $x = 0.02$ and 0.04 [see Figs. 2(a) and 2(b)].

B. Increasing Cr content: Influence of the Cr environment and local spin canting

When x increases in the range $0 < x \leqslant 0.15$, $|\mu_{Cr}|$ strongly decreases, whereas μ_{Fe} shows a rounded maximum below x_C [Figs. 6(b) and 6(c)]. The decrease of $|\mu_{Cr}|$ is linear in the studied series [Fig. 6(b)].

As shown in the Supplemental Material [55], this decrease is directly connected with the number of Cr neighbors, which can be tuned by the concentration or by a proper heat treatment. For $x = 0.15$, $|\mu_{Cr}|$ decreases when Cr clustering is enhanced, either by decreasing the annealing temperature or by increasing the annealing time [Fig. 4(d)].

The huge influence of its environment on a Cr moment was already pointed out in previous calculations [4,27]. It is shown by the shaded region in Fig. 6(a), overlapping different atomic distributions where dispersed Cr atoms have moment magnitudes larger than clustered ones. More precisely, our calculations performed with the same ASRO as in the studied samples yield a strong dependence $\mu_{Cr}(x)$ as in the experiment, but the calculated $|\mu_{Cr}|$ is systematically larger than the experimental one [Fig. 6(b)]. For $x = 0.15$, calculation and experiments performed for several heat treatments exhibit the same systematic tendency [55], but the calculated $|\mu_{Cr}|$ is about twice larger than the measured one.

To resolve this discrepancy we consider a new possibility, namely a *canting* of the Cr moments. This canting could naturally arise from the influence of Dzyaloshinskii-Moryia interactions, as well as from frustrated local configurations, but it was not considered in the experimental or theoretical descriptions discussed so far. The first-principles calculations assume collinear moments, and their evaluation of $|\mu_{Cr}|$ corresponds to the average moment length M. Conversely, in the diffuse scattering experiment, Eqs. (1)–(4) assume a FM collinear alloy, so that only the longitudinal M_Z component (along the magnetic field or along the domain magnetization in zero field) is involved in the expressions of the magnetic cross section. The analysis performed within the linear Marshall's model [35,36] also assumes collinear moments.

We evaluate the influence of a spin canting as follows. As shown in the Supplemental Material [55], locally canted Cr moments $\mathbf{M}$, with transverse spin components M_T (defined so as $M_T^2 = M^2 - M_Z^2$) randomly distributed in space, yield an extra contribution of magnetic origin to the incoherent cross section defined in Eqs. (4) and (5). This contribution writes

$$\left(\frac{d\sigma}{d\Omega}\right)^{M}_{inc} = x\left(\frac{\gamma e^2}{2m_e c^2}\right)^2 M_T^2. \tag{16}$$

The fact that the incoherent cross section measured experimentally is slightly larger than the calculated one, and that this difference increases with x [Fig. 7(a)], justifies the attribution of this deviation to a spin canting. In the simplest case, we assume that only the Cr moments are canted [Fig. 7(b)] and we deduce their canting angle θ directly from this deviation [inset Fig. 7(b)]. A more realistic scenario involves also a canting of the Fe moments neighbors of the Cr ones, but then the Cr and Fe canting angles cannot be determined separately. As an example, we show in Fig. 5 of Ref. [55] the moments deduced by assuming equal Cr and Fe contributions to the incoherent magnetic cross section. The Cr canting angle is reduced, whereas the Fe canting angle remains below 8 deg. In any case, by introducing a spin canting, $|\mu_{Cr}|$ agrees much better with all first-principles calculations. In the dilute limit however, the canting, hardly detected in the incoherent cross section, cannot explain deviations between experiment and theories.

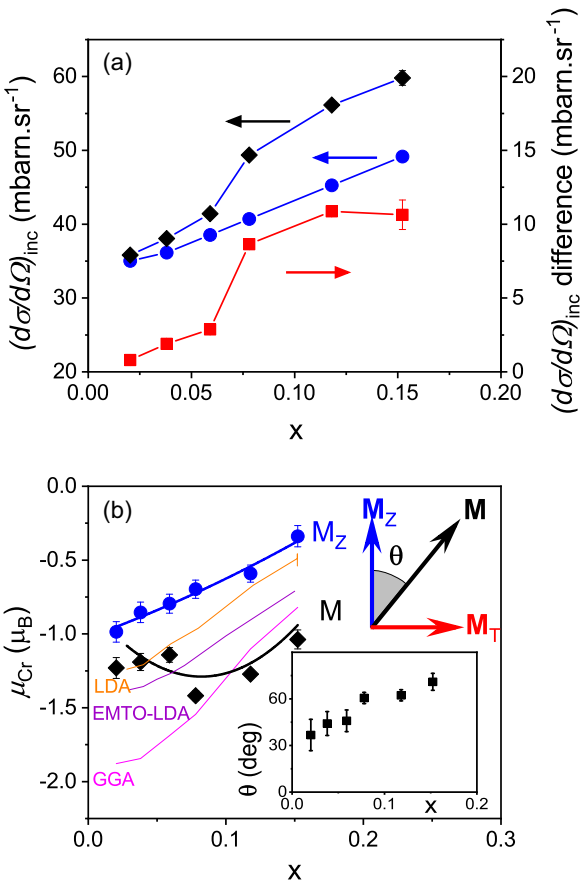

FIG. 7. $Fe_{1-x}Cr_x$ alloys. (a) Variation of the incoherent cross section with concentration x. The difference (red squares) between the fitted (black lozenges) and calculated (blue bullets) cross sections is attributed to a magnetic incoherent cross section σ_{inc}^{M} arising from a random canting of the Cr/Fe moments. (b) Cr moment calculated versus x assuming Cr canting only, with longitudinal M_Z (blue) and transverse M_T moment components. The Cr moment magnitude M (black lozenges) given by $M^2 = M_Z^2 + M_T^2$ is compared with the first-principles calculations: EMTO-LDA from Ruban [25] (purple line), LDA (orange line), and GGA (magenta line) this work. The canting angle θ is plotted in the inset. Thick solid lines are guides to the eye.

Together with the spin canting, μ_{Fe} shows a maximum around $x_1 = 0.06$. This maximum is reproduced by the first-principles calculations, which yield the local perturbations on Fe and Cr sites separately and help clarifying this behavior. For $x < x_R = 0.04$, the Cr atoms fully repel each other in the first two neighbor shells: the ASRO parameters have their maximum negative value: $\alpha_{12} \sim -x/(1-x)$. These dilute alloys are not frustrated since all magnetic interactions are satisfied. The Fe moment increases because of the dominant contribution of its fourth and fifth Cr neighbors. Due to the large $z_{45} = 32$ (as compared with $z_{12} = 14$ and $z_3 = 12$), the perturbation $G(0) = d\mu_{Fe}/dx$ is positive at low x values. As shown in Fig. 5 and in the Supplemental Material [55], $G(0)$ changes sign for $x_1 \sim 0.06$, in good agreement with the maximum of μ_{Fe}.

The spin canting and maximum of μ_{Fe} at x_1 are linked with a maximum of the Curie temperature [64,67]. All features reflect the onset of magnetic frustration induced by the competition of FM Fe-Fe, AFM Cr-Cr, and Cr-Fe near neighbor interactions. The concentration $x = 0.0625$ corresponds to the ordered heterostructure $Fe_{15}Cr_1$, where Cr atoms take the corner sites of a cubic superstructure constructed of $2 \times 2 \times 2$ unit cells. In such case, Cr-Cr pairs are avoided up to the fifth neighbors, and all magnetic interactions are satisfied simultaneously. The resulting AFM structure is collinear and stabilized by a minimum of the spin down density of state at the Fermi energy [68]. In our quenched alloys, near neighbor Cr-Cr pairs start to appear in the first two shells between x_R and x_1, although in a lower amount than in the random case. Competing Cr-Fe and Cr-Cr magnetic interactions induce frustration, spin canting, and a decrease of the M_Z components of the magnetic moments. Above x_C most local configurations are frustrated, due the high Cr content and Cr clustering tendency. μ_{Cr} becomes quite small and μ_{Fe} strongly decreases. For $x = 0.15$, a similar scenario explains how μ_{Cr} decreases with increasing Cr clustering [55].

C. Towards the Cr-rich phase: Reentrant spin glasses and Cr antiferromagnetism

The spin canting observed here is precursor of stronger frustration effects observed in the Cr-rich bcc solid solutions ($x \geqslant 0.7$). It is predicted by first-principles calculations [80] in interfaces [81] or in nanoclusters of concentrated alloys [82]. In bulk materials, canted phases are observed around $x \sim 0.8$. The competition of AFM Cr-Cr and Cr-Fe interactions coexisting with FM Fe-Fe interactions leads to a very original (T, x) magnetic phase diagram [83], showing two reentrant spin glass (RSG) phases with either F or AF dominant character, and one classical spin glass (SG) phase in between. Such frustrated phases have been widely studied in metallic alloys (for a review see Ref. [84]). As a general feature, the magnetic moments cant to minimize the magnetic energy, which shows a macroscopic degeneracy. The RSG phases are mixed phases where SRO transverse spin components coexist with LRO longitudinal components. Under applied field, vortexlike defects where the transverse components rotate over finite length scales (1–10 nm) have been observed in FM-RSG systems [85–87], likely nucleated by the strongest AF pairs. They were recently characterized in a NiMn single crystal by combining small angle neutron scattering with MC simulations [88]. The $Fe_{1-x}Cr_x$ system provides an interesting opportunity to investigate such topological defects. They should be observed for $0.7 \leqslant x \leqslant 0.81$, then disappear in the narrow SG phase ($0.81 \leqslant x \leqslant 0.84$) where the average magnetic interaction vanishes. In the mirrorlike AFM-RSG phase ($0.84 \leqslant x \leqslant 0.9$), solitonlike defects could be nucleated in the AFM medium by FM Fe-Fe pairs. Here they would compete with the spin-density waves of the modulated AF order of Cr, stabilized for $0.84 \leqslant x \leqslant 1$.

Finally, we notice that transverse spin components flip the neutron spins [89], whereas the incoherent scattering due to isotopic disorder and the longitudinal magnetic scattering analyzed in Marshall's formalism do not. So it may be possible to isolate the transverse spin contribution by analyzing the polarization of the scattered neutron beam.

V. CONCLUSION

Our neutron diffuse scattering experiments combined with first-principles calculations show a strong interplay of atomic and magnetic short range orders in $Fe_{1-x}Cr_x$ bcc alloys ($x \leqslant 0.15$). This yields subtle effects as Cr concentration increases, which can be described at a microscopic level. The Cr and Fe magnetic moments strongly depend on the local atomic configurations. For $x \leqslant x_C = 0.11$, band ferromagnetism favors heterocoordination. Cr atoms repel their Cr neighbors to keep the large negative moment induced by a virtual bound state. Full repulsion is achieved only for $x < x_R = 0.04$, then Cr-Cr near neighbor pairs start to appear yielding magnetic frustration. $|\mu_{Cr}|$ decreases and μ_{Fe} shows a maximum at $x_1 \sim 0.06$. Above x_1, moments strongly cant due to the competition of near neighbor interactions. Increasing concentration further above x_C, Cr atoms locally segregate, enhancing the magnetic frustration. The canting observed in the Fe-rich bcc phase anticipates stronger frustration effects in the Cr-rich bcc phase ($0.7 \leqslant x \leqslant 0.9$) where reentrant spin glass phases are stabilized and vortexlike defects expected, prior to the onset of Cr band antiferromagnetism.

The method developed in this paper can be used to investigate short range orders in other ferromagnetic alloys, and extended to dilute alloys with antiferromagnetic or spin glasslike local environments. Precursor effects of segregation can be also studied in bulk alloys at the borderline of a miscibility gap or under irradiation. One could for instance characterize the evolution of chemical order with thermal ageing or under irradiation quantitatively, and study the impact on the magnetic order at the scale of interatomic distances.

The interplay of magnetic and nuclear short range orders in $Fe_{1-x}Cr_x$ alloys results in quasirandom solid solutions for concentrations close to x_c. The stability of the microstructure under thermal ageing or irradiation is used in steels developments, such as the reduced activation ferritic/martensitic steel Eurofer'97, prominent material for fusion devices.

ACKNOWLEDGMENTS

We thank F. Gautier and A. V. Ruban for stimulating discussions and for a critical reading of the manuscript, and S. Michaud for her participation in the experiment. This work was partly supported by the French-German ANR-DFG MAGIKID project. Calculations were performed using DARI-GENCI resources under the A0050906020 project and the CINECA-MARCONI supercomputer within the SISTEEL project.

[1] I. Cook, Nat. Mater. **5**, 77 (2006).
[2] R. L. Klueh and A. T. Nelson, J. Nucl. Mater. **371**, 37 (2007).
[3] J. Wallenius, P. Olsson, C. Lagerstedt, N. Sandberg, R. Chakarova, and V. Pontikis, Phys. Rev. B **69**, 094103 (2004).
[4] T. P. C. Klaver, R. Drautz, and M. W. Finnis, Phys. Rev. B **74**, 094435 (2006).
[5] M. Levesque, E. Martinez, C.-C. Fu, M. Nastar, and F. Soisson, Phys. Rev. B **84**, 184205 (2011).
[6] I. Mirebeau, M. Hennion, and G. Parette, Phys. Rev. Lett. **53**, 687 (1984).
[7] I. Mirebeau and G. Parette, Phys. Rev. B **82**, 104203 (2010).
[8] N. P. Filipova, V. A. Shabashov, and A. L. Nicolaev, Phys. Metals Metall. **90**, 145 (2000).
[9] A. Froideval, R. Iglesias, M. Samaras, S. Schuppler, P. Nagel, D. Grolimund, M. Victoria, and W. Hoffelner, Phys. Rev. Lett. **99**, 237201 (2007).
[10] F. Ducastelle and F. Gautier, J. Phys. F **6**, 2039 (1976)
[11] F. Ducastelle and G. Tréglia, J. Phys. F **10**, 2137 (1980).
[12] A. Bieber and F. Gautier, Solid State Commun. **38**, 1219 (1981).
[13] J. Friedel, *The Physics of Metals*, edited by J. M. Ziman, (Cambridge University Press, Cambridge, 1969).
[14] M. Hennion, J. Phys. F **13**, 2351 (1983).
[15] J. Friedel, Nuovo Cimento **7**, 287 (1958).
[16] I. A. Campbell, Proc. Phys. Soc. **89**, 71 (1966).
[17] I. A. Campbell and A. A. Gomes, Proc. Phys. Soc. London **91**, 319 (1967).
[18] A. Caro, D. A. Crowson, and M. Caro, Phys. Rev. Lett. **95**, 075702 (2005).
[19] M. Yu. Lavrentiev, R. Drautz, D. Nguyen-Manh, T. P. C. Klaver, and S. L. Dudarev, Phys. Rev. B **75**, 014208 (2007).
[20] P. Olsson, J. Wallenius, C. Domain, K. Nordlund, and L. Malerba, Phys. Rev. B **72**, 214119 (2005).
[21] P. Olsson, C. Domain, and J. Wallenius, Phys. Rev. B **75**, 014110 (2007).
[22] P. Erhart, B. Sadigh, and A. Caro, Appl. Phys. Lett. **92**, 141904 (2008).
[23] For a review see L. Malerba, A. Caro, and J. Wallenius, J. Nucl. Mater. **382**, 112 (2008).
[24] P. E. A. Turchi, L. Reinhard, and G. M. Stocks, Phys. Rev. B **50**, 15542 (1994).
[25] A. V. Ruban, P. A. Korzhavyi, and B. Johansson, Phys. Rev. B **77**, 094436 (2008).
[26] P. A. Korzhavyi, A. V. Ruban, J. Odqvist, J. O. Nilsson, and B. Johansson, Phys. Rev. B **79**, 054202 (2009).
[27] O. E. Peil, A. V. Ruban, and B. Johansson, Phys. Rev. B **85**, 165140 (2012).
[28] A. T. Paxton and M. W. Finnis, Phys. Rev. B **77**, 024428 (2008).
[29] D. Nguyen-Manh and S. L. Dudarev, Phys. Rev. B **80**, 104440 (2009).
[30] R. Soulairol, C. Barreteau, and C.-C. Fu, Phys. Rev. B **94**, 024427 (2016).
[31] A. V. Ruban and V. I. Razumovskiy, Phys. Rev. B **86**, 174111 (2012).
[32] A. V. Ponomareva, A. V. Ruban, O. Yu. Vekilova, S. I. Simak, and I. A. Abrikosov, Phys. Rev. B **84**, 094422 (2011).
[33] V. I. Razumovskiy, A. V. Ruban, and P. A. Korzhavyi, Phys. Rev. Lett. **107**, 205504 (2011).
[34] R. N. Hajra, S. Raju, A. K. Rai, H. Tripath, S. Saroja, and T. Jayakumar, Adv. Mater. Res. **794**, 468 (2013).
[35] W. Marshall, J. Phys. C **1**, 88 (1968).
[36] F. Gautier, Ann. Phys. **14**, 251 (1973).
[37] R. A. Medina and J. W. Cable, AIP Conf. Proc. **29**, 292 (1976).
[38] R. A. Medina and J. W. Cable, Phys. Rev. B **15**, 1539 (1977).
[39] C. G. Shull and M. K. Wilkinson, Phys. Rev. **97**, 304 (1955).

[40] M. F. Collins and G. G. Low, J. Phys. Paris **25**, 596 (1964).
[41] F. Kajzar and G. Parette, Phys. Rev. B **22**, 5471 (1980).
[42] M. F. Collins and G. G. Low, Proc. Phys. Soc. **86**, 535 (1965).
[43] A. T. Aldred, B. D. Rainford, J. S. Kouvel, and T. J. Hicks, Phys. Rev. B **14**, 228 (1976).
[44] G. Frollani, F. Menzinger, and F. Sacchetti, Phys. Rev. B **11**, 2030 (1975).
[45] F. Sacchetti, Solid State Commun. **34**, 265 (1980).
[46] B. Drittler, N. Stefanou, S. Blugel, R. Zeller, and P. H. Dederichs, Phys. Rev. B **40**, 8203 (1989).
[47] J. O. Anderson and B. Sundman, Calphad **11**, 83 (1987); O. Kubachevski and S. B. Olkokk, *Metallurgical Thermochemistry* (Springer, Berlin, 1979).
[48] D. A. Vasilev and A. L. Udovskii, Russian Metal. **2016**, 443 (2016).
[49] E. Balanzat and J. Hillairet, J. Phys. F **11**, 1977 (1981).
[50] V. Pierron-Bohnes, I. Mirebeau, E. Balanzat, and M. C. Cadeville, J. Phys. F **14**, 197 (1984).
[51] S. Novy, P. Pareige, and C. Pareige, J. Nucl. Mater. **384**, 96 (2009).
[52] K. D. Rouse and M. J. Cooper, Acta Crystallogr. Sect. A **26**, 682 (1970).
[53] A. W. Hewatt, Acta Crystalloge. Sect. A **35**, 248 (1979).
[54] I. A. Blech and B. L. Averbach, Phys. Rev. **137**, A1113 (1965).
[55] See Supplemental Material at http://link.aps.org/supplemental/10.1103/PhysRevB.100.224406 for details on experimental corrections of neutron data, magnetization measurements, environmental effects in first-principles calculations, and calculation of the incoherent magnetic cross section due to spin canting.
[56] H. R. Child and J. W. Cable, Phys. Rev. B **13**, 227 (1976).
[57] W. Marshall and S. W. Lovesey, *Theory of Thermal Neutron Scattering* (Oxford Clarendon, London, 1971).
[58] J. M. Cowley, Phys. Rev. **77**, 669 (1950).
[59] R. E. Watson and A. J. Freeman, Acta Crystallogr. **14**, 27 (1961).
[60] A. T. Aldred, Phys. Rev. B **14**, 219 (1976).
[61] M. Furusaka, Y. Ishikawa, S. Yamaguchi, and Y. Fujino, Physica B (Amsterdam) **120**, 383 (1983).
[62] F. Bley, Acta Metal. Mater. **40**, 1505 (1992).
[63] E. Martinez, O. Senninger, C.-C. Fu, and F. Soisson, Phys. Rev. B **86**, 224109 (2012).
[64] J. B. J. Chapman, P.-W. Ma, and S. L. Dudarev, Phys. Rev. B **99**, 184413 (2019).
[65] M. Hennion, D. Ronzaud, and P. Guyot, Acta Metal. **30**, 599 (1982).
[66] F. Soisson and T. Jourdan, Acta Mater. **103**, 870 (2016).
[67] M. Y. Lavrentiev, K. Mergia, M. Gjoka, D. Nguyen-Manh, and G. Apostolopoulos, J. Phys.: Condens. Matter **24**, 326001 (2012).
[68] D. Nguyen-Manh, M. Y. Lavrentiev, and S. L. Dudarev, C. R. Phys. **9**, 379 (2008).
[69] P. E. Blochl, Phys. Rev. B **50**, 17953 (1994).
[70] G. Kresse and D. Joubert, Phys. Rev. B **59**, 1758 (1999).
[71] G. Kresse and J. Hafner, Phys. Rev. B **47**, 558 (1993).
[72] G. Kresse and J. Furthmüller, Comput. Mat. Sci. **6**, 15 (1996).
[73] G. Kresse and J. Furthmuller, Phys. Rev. B **54**, 11169 (1996).
[74] J. P. Perdew, K. Burke, and M. Ernzerhof, Phys. Rev. Lett. **77**, 3865 (1996).
[75] Yu. I. Petrov, E. A. Shafranovsky, Yu. F. Krupyanskii, and S. V. Essine, J. Appl. Phys. **91**, 352 (2002).
[76] H. J. Monkhorst and J. D. Pack, Phys. Rev. B **13**, 5188 (1976).
[77] M. Methfessel and A. T. Paxton, Phys. Rev. B **40**, 3616 (1989).
[78] A. J. P. Meyer and G. Ash, J. Appl. Phys. **32**, S330 (1961).
[79] S. Chadov, J. Minar, M. I. Kastnelson, H. Ebert, D. Kodderitzsch, and A. I. Lichtenstein, Europhys. Lett. **82**, 37001 (2008).
[80] R. Soulairol, C.-C. Fu, and C. Barreteau, Phys. Rev. B **84**, 155402 (2011).
[81] M. Yu. Lavrentiev, R. Soulairol, C.-C. Fu, D. Nguyen-Manh, and S. L. Dudarev, Phys. Rev. B **84**, 155203 (2011).
[82] C.-C. Fu, M. Y. Lavrentiev, R. Soulairol, S. L. Dudarev, and D. Nguyen-Manh, Phys. Rev. B **91**, 094430 (2015)
[83] S. K. Burke, R. C. Cywinski, and J. R. Davis, J. Phys. F **13**, 451 (1983).
[84] M. J. P. Gingras, *Competition Between Ferromagnetic and Spin Glass Order in Random Magnets: The Problem of Reentrant Spin Glasses* (World Scientific, Singapore, 1994), pp. 238–285.
[85] M. Hennion, I. Mirebeau, B. Hennion, S. Lequien, and F. Hippert, Europhys. Lett. **2**, 393 (1986).
[86] P. Boeni, S. Shapiro, and K. Motoya, Solid State Commun. **60**, 881 (1986).
[87] S. Lequien, I. Mirebeau, M. Hennion, B. Hennion, F. Hippert, and A. P. Murani, Phys. Rev. B **35**, 7279 (1987).
[88] I. Mirebeau, N. Martin, M. Deutsch, L. J. Bannenberg, C. Pappas, G. Chaboussant, R. Cubitt, C. Decorse, and A. O. Leonov, Phys. Rev. B **98**, 014420 (2018).
[89] R. M. Moon, T. Riste, and W. C. Koehler, Phys. Rev. **181**, 920 (1969).

Magnetic and atomic short range order in $Fe_{1-x}Cr_x$ alloys.

I. Mirebeau[1], V. Pierron-Bohnes[2], C. Decorse[3], E. Rivière[3], Chu-Chun Fu[4], Kangming Li[4], G. Parette[1], N. Martin[1]
[1] *Laboratoire Léon Brillouin, CEA-CNRS, Université Paris-Saclay, CEA-Saclay, F-91191 Gif-sur-Yvette, France*
[2] *Université de Strasbourg, CNRS, Institut de Physique et Chimie des Matériaux de Strasbourg (IPCMS), UMR 7504, F-67000 Strasbourg, France*
[3] *ICMMO, Université Paris-Sud, Université Paris-Saclay, F-91405 Orsay France and*
[4] *DEN-Service de Recherches de Métallurgie Physique, CEA, Université Paris-Saclay, F-91191 Gif-sur-Yvette France*
(Dated: November 6, 2019)

In this supplemental material, we give details about the experimental corrections in the neutron scattering experiment (section I), the magnetization measurements (section II), the environmental effects in first-principles calculations (section III), and the expression of the neutron magnetic cross section in the case of a spin canting (section IV).

I. NEUTRON SCATTERING CROSS SECTION : EXPERIMENTAL CORRECTIONS

To determine the neutron cross sections in absolute scale, the raw intensities were corrected for background and calibrated by measuring Vanadium (V), which is a strong incoherent scatterer and cadmium (Cd), which is a strong absorber, as well as the empty equipment (E). The V and Cd standards were carved with the same shape and volume as the samples to minimize the corrections. All intensities are recorded for the same number of incident neutrons.

The intensity N_{cor} corrected from background is deduced from the raw intensity N by the expression:

$$N_{cor} = N - N_{Cd} - A(0)\left[N_E - N_{Cd}\right] \tag{1}$$

where N_{Cd} and N_E are the raw intensities scattered by the Cd standard and the empty equipment respectively. $A(0)$ is the transmission, namely the absorption factor $A(\theta)$ at zero scattering angle. The absorption factor of a cylindrical sample of radius R and height h ($R \ll h$) is calculated by the expression[1,2]:

$$A(\theta) = \exp\left[-\left(a_1 + b_1 sin^2\theta\right)\mu R + \left(a_2 + b_2 sin^2\theta\right)(\mu R)^2\right] \tag{2}$$

where a_1, b_1, a_2, b_2 are numerical constants, 2θ is the scattering angle, and $\mu = n.\sigma_T$ is the mass absorption coefficient, product of the density n and total cross section σ_T. The same corrections apply to the measured sample (S) and to the V standard.

The neutron cross section of the sample is then calculated in absolute scale by the expression:

$$\left(\frac{d\sigma}{d\Omega}\right) = \frac{\sigma_{inc}^V}{4\pi}\frac{n_V A_V(\theta)\left(1-\delta_S^{'}\right)}{n_S A_S(\theta)\left(1-\delta_V^{'}\right)}\frac{N_{cor}^S}{N_{cor}^V} \tag{3}$$

where σ_{inc}^V=5.07 barn is the incoherent scattering cross section of vanadium. n_S and n_V are the S and V densities, taking into account that S and V have the same volume in the neutron beam. A_S and A_V are the absorption coefficients. The multiple scattering coefficients $\delta^{'}$ are calculated following ref.3, knowing the quantities μR and R/h.

The large incident neutron wavelength (λ= 4.75Å) ensures the absence of any Bragg peak and therefore of double Bragg diffraction. Moreover, since all samples and standards are measured at low temperature (8 K), the contribution of inelastic scattering is negligible for all scattering angles. This was checked by performing an energy analysis of some neutron patterns.

These corrections and calibrations have been performed for all samples in all configurations of the magnetic field and neutron polarization. Combining the cross sections measured in different configurations yields the nuclear, magnetic and nuclear-magnetic interference cross sections, as described in Sec. II.B of the main text.

II. MAGNETIZATION MEASUREMENTS

To measure the bulk magnetization, small spheres of about 2 mg were cut in the samples used for diffuse scattering measurements. The error bar on the mass was estimated to 0.01 mg. The magnetization was measured using a SQUID magnetometer at 5 K under an external magnetic field up to 6 T. The curves were corrected from the demagnetizing field and the saturated part extrapolated linearly to zero to get the average moment $\bar{\mu}$. An iron sample of the same

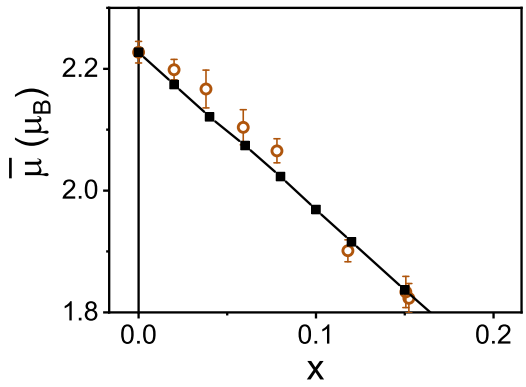

FIG. 1: $Fe_{1-x}Cr_x$ alloys. Average moment $\bar{\mu}$ versus concentration x measured on pieces of the samples measured by neutron scattering (brown circles), and reported by Aldred[4] on samples quenched from 825 °C (black squares).

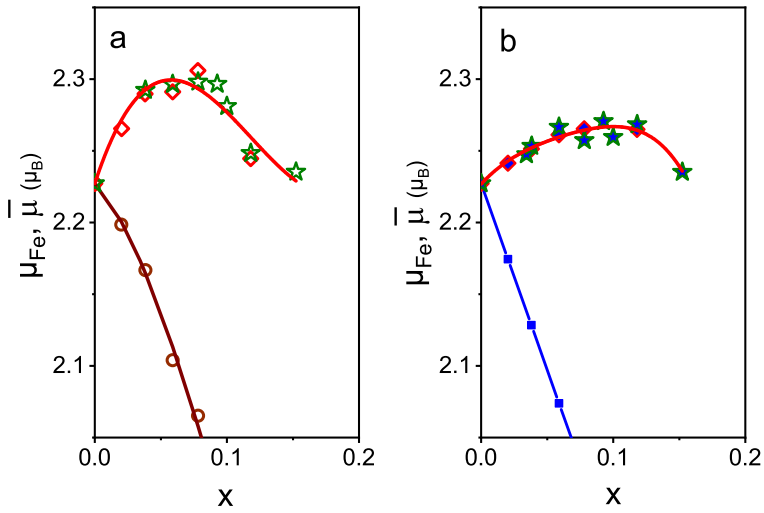

FIG. 2: $Fe_{1-x}Cr_x$ alloys. Influence of the average moment value $\overline{\mu}(x)$ on the determination of the Fe moment μ_{Fe}. (a) Magnetization (circles) measured using SQUID (this work) on ASRO samples measured by neutrons and μ_{Fe} deduced. (b) Average moment (squares) measured by Aldred[4] on quenched samples and μ_{Fe} deduced. To determine μ_{Fe}, the quantity $\Delta\mu = \mu_{Cr} - \mu_{Fe}$ determined from neutron diffuse scattering in ASRO samples is used in both cases. Polarized neutrons (lozenges); unpolarized neutrons (stars). Whatever $\overline{\mu}(x)$ is used, a maximum of $\mu_{Fe}(x)$ is observed with an increase of 2-3% for $x < 0.1$. Lines are guides to the eye.

size and purity was measured for normalization. Measurements and calibrations were performed several times to check the reproducibility and estimate the error bar on the magnetization in absolute units, which is of the order of 1%, including the error on the sample position.

Fig. 1 compares the magnetization in our samples (annealed down to 430 °C and quenched) those of Aldred[4] (quenched from 825 °C). Our samples show atomic short range order (ASRO), where the ASRO parameter α_{12} on the first two shells surrounding a Cr atom is close to its maximum negative value $\alpha_{12} \sim -x/(1-x)$ for $x \leq 0.04$. On the other hand, the atomic distribution in the samples measured by Aldred is closer to random (see Tab. I of the main text). The figure suggests a small but systematic effect of the ASRO on the average moment, this effect being more pronounced at low concentration. Namely, below x_c our data points situate above those of Aldred, suggesting that μ_{Fe} increases with increasing the amount of ASRO, and that this enhancement counteracts the influence of the negative moment μ_{Cr}.

The concentration dependencies of the average magnetic moments $\mu_{Fe}(x)$ and $\mu_{Cr}(x)$ can be deduced by combining

neutrons data, which measure $\Delta\mu = \mu_{Cr} - \mu_{Fe}$, and magnetization data, which measure $\overline{\mu} = x\mu_{Cr} + (1-x)\mu_{Fe}$.

In Fig. 2, we show $\mu_{Fe}(x)$ obtained by combining our neutron data with the magnetization data measured on the same samples (a) and magnetization measured on quasi random alloys[4](b). μ_{Fe} shows a maximum versus x in both cases, at a concentration slightly below $x_c = 0.10$. This maximum is more pronounced in case (a). It is well reproduced by first-principles calculations performed on samples with same ASRO state, as shown in the main text. μ_{Cr} is the same in both cases.

III. ENVIRONMENTAL EFFECTS IN FIRST-PRINCIPLES CALCULATIONS

The DFT simulations on these samples provide the position, atomic nature $X(m)$, and moment $\mu(m)$ of each atom m. To obtain the magnetic perturbations due to Cr neighbors, the first step was, for each atom m, to determine $n_i(m)$, the number of Cr atoms in its i^{th} neighbor shell. Periodic conditions have been applied to the box when the neighbors of m were out of the initial box. Due to the size of the box, the upper limit for i was $i = 9$ (so that the z_i neighbors of a given atoms are all different). In a second step, for each i and each x, we plotted $\mu(m)$ as a function of $n_i(m)$ for all m atoms with $X(m) =$ Fe (resp. $X(m) =$ Cr). The calculated parameters g_i and h_i are the slopes of the linear fits of these plots, performed for each concentration. The MSRO parameters ϕ_i combine the perturbations g_i induced by a Cr moment on its neighboring Fe moments at the i^{th} shell and the perturbations h_i on its neighboring Cr moments[8,9] (see Eq. 13 of the main text). Examples of such plots are shown in Fig. 3 for the sample $Fe_{0.85}Cr_{0.15}$ annealed at 430 °C for 84 h, which shows many types of configurations.

In Marshall's model[8], keeping the first order terms of the concentration dependence and neglecting the effect of ASRO, one can write:

$$\frac{d\mu_{Fe}}{dx} = G(0) = \sum_i z_i g_i \tag{4}$$

$$\frac{d\mu_{Cr}}{dx} = H(0) = \sum_i z_i h_i. \tag{5}$$

and

$$\frac{d\overline{\mu}}{dx} = \mu_{Cr} - \mu_{Fe} + \sum_i z_i \phi_i. \tag{6}$$

In Fig. 4, the sums $G(0)$ and $H(0)$ deduced from the g_i and h_i parameters calculated above are plotted versus x, showing that Eqs. 4 and 5 are verified. $G(0)$ is positive at low concentration and changes sign around $x = 0.05$, in agreement with the variation of μ_{Fe} which shows a maximum at about the same concentration (Fig. 6c of the main text). Similarly $H(0)$ is positive and constant within the error bars, in agreement with the linear increase of μ_{Cr} (Fig. 6b of the main text). The calculated slopes are in good agreement with the experimental ones. Eq.6 is also verified within the statistical accuracy.

IV. MAGNETIC DIFFUSE SCATTERING DUE TO SPIN CANTING

As discussed in the main text, a local canting of the magnetic moments could explain the observed excess of incoherent scattering (see Fig. 7 therein). In this context, canting reflects the existence of moment component M_{T} in the (x, y)-plane, perpendicular to the z-direction which is that of the spontaneous domain magnetization (in zero applied field) or of the magnetization induced by an applied magnetic field (M_{Z}). In both cases, we expect the moments orientations to remain uncorrelated in the (x, y)-plane, leading to a random distribution of M_{T}. In what follows, we show that the contribution of M_{T} to the measured scattering cross sections can be actually derived from the case of a paramagnetic sample in a magnetic field. This analogy is natural since a paramagnet will then be appreciably polarized at low temperature (*i.e.*, showing a finite $\langle M_Z^2 \rangle$), while remaining globally disordered (*i.e.*, with a random M_T).

A. Differential magnetic scattering cross section of a paramagnet under an applied magnetic field

Following Ref. 7 and using the definition $\mathbf{M} = g\,\mu_{\mathrm{B}}\,\mathbf{S}$ (where $\mathbf{S}$ is the spin operator), the general expression for the differential magnetic scattering cross section of a paramagnet reads

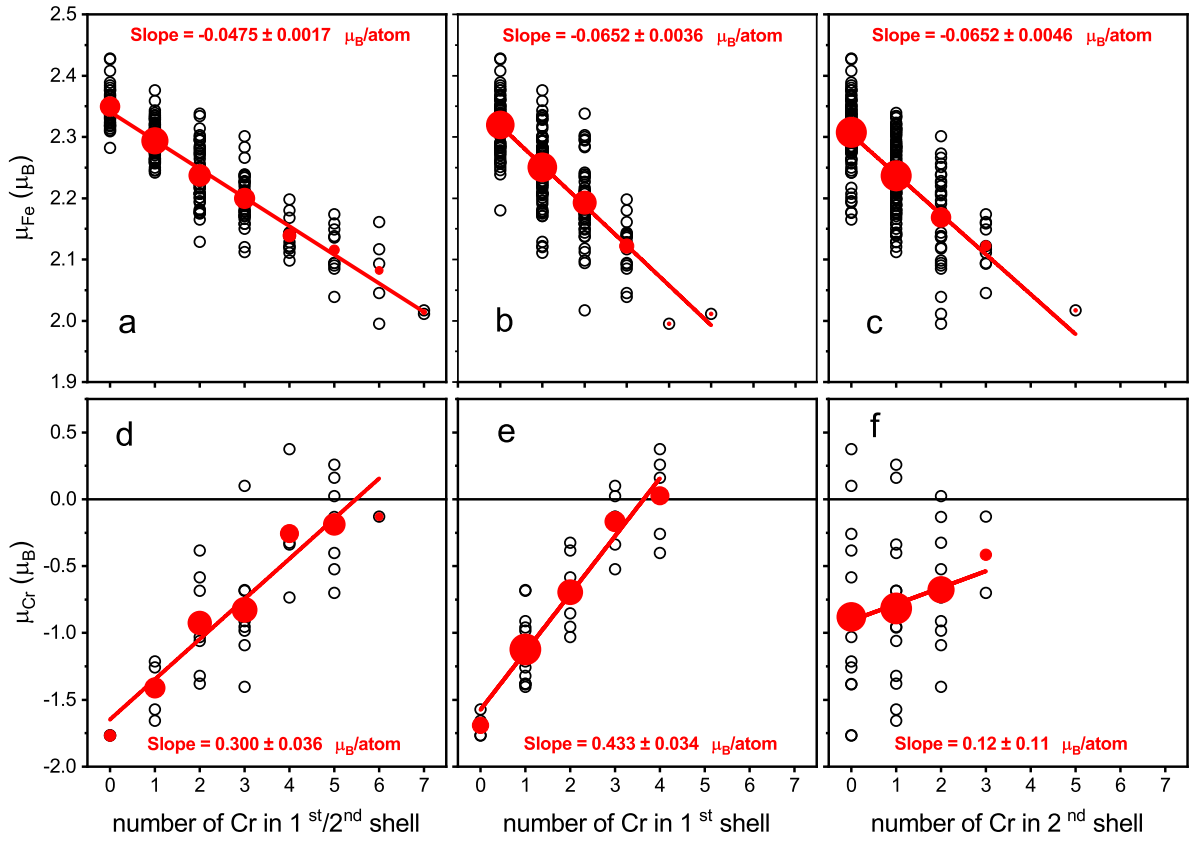

FIG. 3: $Fe_{1-x}Cr_x$ sample with x=0.1506, annealed at 430 °C for 84 h. Magnetic moment dependence with the number of Cr in the first two neighbor shells deduced from DFT. (a,b,c) Fe moments; (d,e,f) Cr moments. Atomic configuration having ASRO parameters close to the experimental one have been considered (Tab. I of the main text). The ASRO for this sample corresponds to the maximum segregation. Black circles: individual magnetic moments. The red circles are averages for a given number of Cr neighbors, and their surface is proportional to the number of atoms obtained. The red line is a linear fit of the average moment dependence with the number of Cr neighbors.

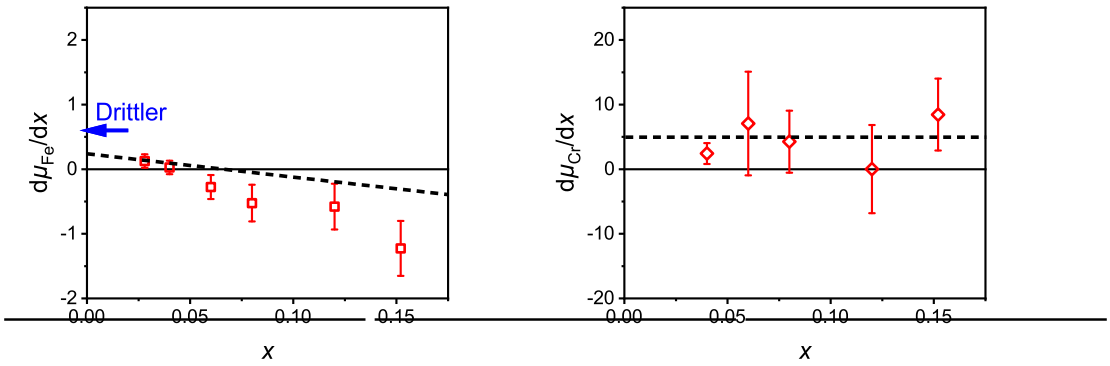

FIG. 4: DFT calculations: (a) Global perturbation $G(0)$ on the Fe sites. The blue arrow shows the results of Drittler[6]. (b) Global perturbation $H(0)$ on the Cr sites. Black dashed lines: experimental slopes $d\mu_{Fe}/dx$ and $d\mu_{Cr}/dx$, deduced from Fig. 6 of the main text.

$$\left(\frac{d\sigma}{d\Omega}\right)_M = \left(\frac{\gamma e^2}{2m_e c^2}\right)^2 F(K)^2 \times \sum_{\alpha,\beta}\left\{(\delta_{\alpha\beta}-\kappa_\alpha\kappa_\beta)\sum_{i,j}\exp\left[i\mathbf{K}\cdot(\mathbf{i}-\mathbf{j})\right]\langle M_i^\alpha M_j^\beta\rangle\right\} \quad , \tag{7}$$

where $\left(\frac{\gamma e^2}{2m_e c^2}\right)^2 = 72.59$ mbarn$\cdot\mu_{\mathrm{B}}^{-2}$, $\mathbf{K}=(K_x,K_y,K_z)$ is the momentum transfer, $F(K)$ the magnetic form factor and $\kappa_\alpha = K_\alpha/|\mathbf{K}|$. The thermal averages $\langle\cdots\rangle$ in Eq. 7 are defined as

$$\langle M_i^\alpha M_j^\beta\rangle = \begin{vmatrix} \langle M_i^\alpha\rangle\langle M_j^\beta\rangle & \text{for} \quad i\neq j \\ \delta_{\alpha\beta}\langle (M_i^\alpha)^2\rangle & \text{for} \quad i=j \end{vmatrix} \quad . \tag{8}$$

Applying a magnetic field along the z-direction breaks the overall symmetry, which yields

$$\begin{array}{l} \langle M_i^x M_j^y\rangle = \langle M_i^x M_j^z\rangle = \langle M_i^y M_j^z\rangle = 0 \\ \langle M_i^x M_j^x\rangle = \langle M_i^y M_j^y\rangle = \delta_{ij}\langle (M_i^x)^2\rangle \\ \langle M_i^z M_j^z\rangle = \langle M_i^z\rangle^2 + \delta_{ij}\left[\langle (M^z)^2\rangle - \langle M^z\rangle^2\right] \end{array} \quad , \tag{9}$$

such that

$$\sum_{\alpha,\beta}(\delta_{\alpha\beta}-\kappa_\alpha\kappa_\beta)\langle M_i^\alpha M_j^\beta\rangle = \left(1+\kappa_z^2\right)\langle M_i^x M_j^x\rangle + \left(1-\kappa_z^2\right)\langle M_i^z M_j^z\rangle \quad . \tag{10}$$

Using Eqs. 8-10, we finally get

$$\sum_{\alpha,\beta}\left\{(\delta_{\alpha\beta}-\kappa_\alpha\kappa_\beta)\sum_{i,j}\exp\left[i\mathbf{K}\cdot(\mathbf{i}-\mathbf{j})\right]\langle M_i^\alpha M_j^\beta\rangle\right\} = \left(1-\kappa_z^2\right)\langle M^z\rangle^2\left|\sum_i\exp\left(i\mathbf{K}\cdot\mathbf{i}\right)\right|^2 + \left(1-\kappa_z^2\right)\left[\langle (M^z)^2\rangle - \langle M^z\rangle^2\right] + \left(1+\kappa_z^2\right)\langle (M_i^x)^2\rangle \quad , \tag{11}$$

where $M^z \equiv M_Z$. The first term in Eq. 11 corresponds to the magnetic coherent scattering (giving rise to Bragg peaks, *e.g.*). The second term is the diffuse scattering due to longitudinal magnetization (modulated by the atomic (ASRO) and magnetic (MSRO) short-range orders in the model of Marshall[8]). The third term originates in the transverse moment components and emulates the case of locally canted magnetic moments. We evaluate this contribution in the following and discuss its relevance to the comparison between the experimental and numerical results presented in the main text.

B. Diffuse scattering due to locally canted magnetic moments

For a $Fe_{1-x}Cr_x$ alloy, we first assume that only the Cr moments are canted. Their transverse component contribute to the differential magnetic scattering cross section as

$$\left(\frac{d\sigma}{d\Omega}\right)_M^T = \left(\frac{\gamma e^2}{2m_e c^2}\right)^2 F(K)^2 \times x\left(1+\kappa_z^2\right)\frac{M_T^2}{2} \quad , \tag{12}$$

using $\langle (M^x)^2\rangle = M_T^2/2$ as a result of averaging within the (x,y)-plane. Considering the usual experimental configuration where the scattering vector is perpendicular to the applied field (*i.e.*, $\kappa_z = 0$), Eq. 12 reduces to

$$\left(\frac{d\sigma}{d\Omega}\right)_M^T\Bigg|_{\mathbf{H}\perp\mathbf{K}} = \left(\frac{\gamma e^2}{2m_e c^2}\right)^2 F(K)^2 \times \frac{x\,M_T^2}{2} \quad . \tag{13}$$

In turn, the zero-field case is derived by averaging out Eq. 12 over all possible orientations of the z-axis (*i.e.*, $\langle\kappa_z^2\rangle = 1/3$), yielding

$$\left(\frac{d\sigma}{d\Omega}\right)_M^T\Bigg|_{\mathrm{H}=0} = \left(\frac{\gamma e^2}{2m_e c^2}\right)^2 F(K)^2 \times \frac{2\,x\,M_T^2}{3} \quad . \tag{14}$$

Neglecting the weak K-dependence of the magnetic form factor[1] (*i.e.*, setting $F(K) = 1$), one can define

$$\left(\frac{d\sigma}{d\Omega}\right)_{inc}^T = x\left(\frac{\gamma e^2}{2m_e c^2}\right)^2 M_T^2 \quad . \tag{15}$$

Then the differential scattering cross sections defined in Eqs. 2-3 of main text become

$$\left(\frac{d\sigma}{d\Omega}\right)_{H=0} = \left(\frac{d\sigma}{d\Omega}\right)_N + \left(\frac{d\sigma}{d\Omega}\right)_{ASRO} + \frac{2}{3}\left(\frac{d\sigma}{d\Omega}\right)_{MSRO} + \frac{2}{3}\left(\frac{d\sigma}{d\Omega}\right)_{inc}^T \quad , \tag{16}$$

in zero-field and

$$\left(\frac{d\sigma}{d\Omega}\right)_{\mathbf{H}\perp\mathbf{K}} = \left(\frac{d\sigma}{d\Omega}\right)_N + \left(\frac{d\sigma}{d\Omega}\right)_{ASRO} + \left(\frac{d\sigma}{d\Omega}\right)_{MSRO} + \frac{1}{2}\left(\frac{d\sigma}{d\Omega}\right)_{inc}^T \quad , \tag{17}$$

under a field applied along the z-direction, where the subscript N refers to the usual nuclear incoherent scattering, due to isotopic and nuclear moment disorder. Interestingly, the contribution from MSRO can be eliminated through a linear combination of Eqs. 16 and 17

$$3\left(\frac{d\sigma}{d\Omega}\right)_{H=0} - 2\left(\frac{d\sigma}{d\Omega}\right)_{\mathbf{H}\perp\mathbf{K}} = \left(\frac{d\sigma}{d\Omega}\right)_N + \left(\frac{d\sigma}{d\Omega}\right)_{ASRO} + \left(\frac{d\sigma}{d\Omega}\right)_T \quad , \tag{18}$$

Thus, a calibration of the measured cross sections in absolute units allows determining M_T from Eq. 15, since the nuclear incoherent term and the Laue scattering (constant contribution to the ASRO) can be calculated accurately using tabulated scattering lengths (see Eqs. 4-7 of main text). Introducing the canting angle $\theta = \arctan(M_T/M_Z)$ of the Cr moments, one can reconcile the measured and calculated incoherent cross sections. We find that θ must vary from 37° for $x = 0.02$ up to 71° for $x = 0.15$, as shown in Fig. 7 of main text.

We note that the above discussion neglects a possible canting of the Fe moments and only yields an upper estimate for θ. In practice, the magnetic coupling between Cr moments and their Fe 1$^{\mathrm{st}}$ and 2$^{\mathrm{nd}}$ neighbors should lead to a local canting of the latter. This implies a modification of Eq. 15, which takes the following form

$$\begin{aligned}\left(\frac{d\sigma}{d\Omega}\right)_{inc}^T &= \left(\frac{\gamma e^2}{2m_e c^2}\right)^2 x\cdot\left\{\left(M_T^{\mathrm{Cr}}\right)^2 + y\left(M_T^{\mathrm{Fe}}\right)^2\right\} \\ &= \left(\frac{\gamma e^2}{2m_e c^2}\right)^2 x\cdot\left\{\left(M_Z^{\mathrm{Cr}}\tan\theta\right)^2 + y\left(M_Z^{\mathrm{Fe}}\tan\theta_{\mathrm{Fe}}\right)^2\right\} \quad ,\end{aligned} \tag{19}$$

[1] An approximation which is justified owing to the explored momentum transfer range, limited to small $\mathbf{K}$.

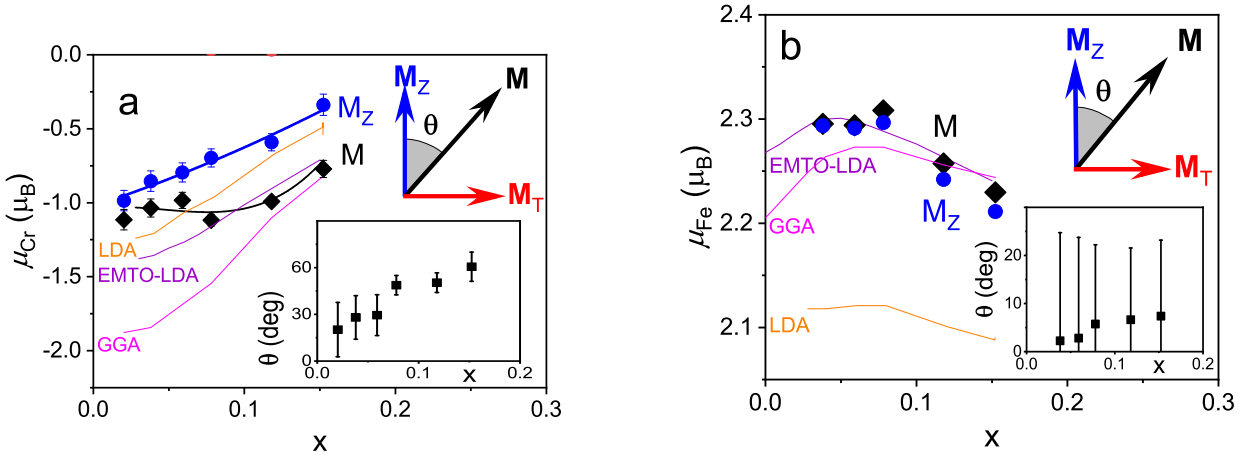

FIG. 5: $Fe_{1-x}Cr_x$ alloys. Cr moment (a) and Fe moment (b) calculated assuming Cr and Fe canting with equal contributions to the incoherent cross section, as described in the text. The moment magnitude M (black lozenges) given by $M^2 = M_Z^2 + M_T^2$ is compared with the first-principles calculations: EMTO-LDA from Ruban[10] (purple line), LDA (orange line) and GGA (magenta line), this work. The canting angle θ is plotted in the inset. Thick solid lines are guides to the eye.

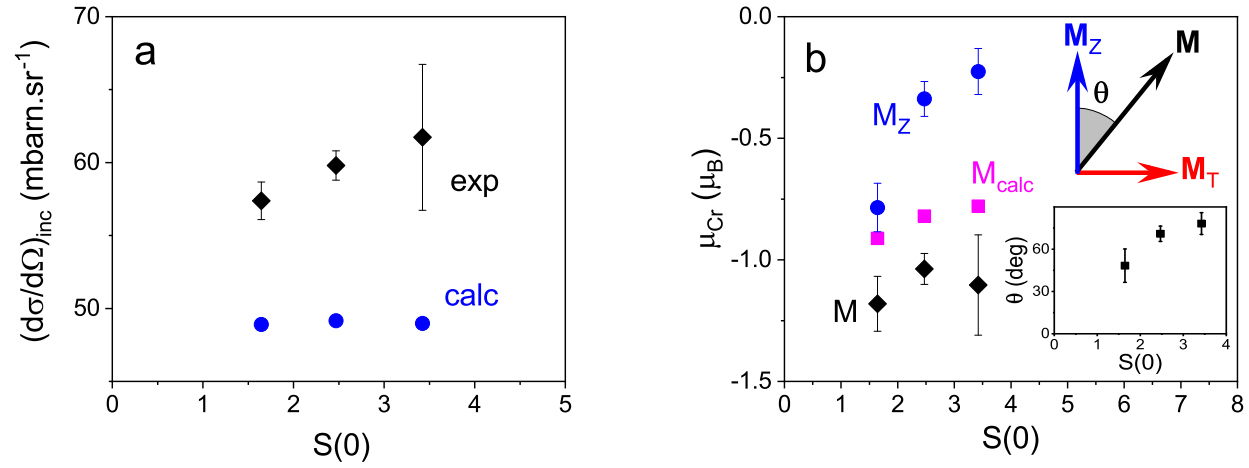

FIG. 6: (a) Variation of the incoherent cross section with clustering tendency, monitored by the ASRO function $S(0)$ (see text and Eq. 7 of main text). The difference between experimental (black lozenges) and calculated (blue bullets) cross sections is attributed to a magnetic incoherent cross section coming from the random canting of the Cr moments. (b) Cr moment μ_{Cr} calculated versus $S(0)$ with this assumption. The Cr moment magnitude M ($M^2 = M_Z^2 + M_T^2$) (black lozenges) is compared with the DFT (GGA) results (magenta squares). The inset shows the corresponding canting angles θ.

where the concentration y varies from $y = 14\,(1-x)\,(1-\alpha_{12})$ at low Cr content (see Eq. 6 of main text) to $y = (1-x)/x$ for $x > x_C$. Eq. 19 illustrates the fact that the contribution of the canted Fe moments will trade off with the one of the Cr moments. In Fig. 5, we show the variations of the canted Cr and Fe moments obtained by assuming equal contributions of Fe and Cr moments to the magnetic incoherent cross section. At $x = 0.15$, a canting angle $\theta_{Fe} = 7°$ (corresponding to $M_T^{Fe} = 0.28\,\mu_B$/Fe and $M_Z^{Fe} = 2.22\,\mu_B$/Fe) yields a differential incoherent magnetic cross section of ≈ 5 mbarn.sr^{-1}, which accounts for about one half of the difference between the measured and calculated values. As a result, θ decreases from 71° (if only the Cr moments are canted) to 50° for $\theta_{Fe} = 7°$. Of course, we note that there exists an infinity of combinations satisfying Eq. 19. However, since we are dealing with $Fe_{1-x}Cr_x$ alloys with $x \ll 1$, θ_{Fe} will always be much smaller than θ.

Strikingly, a similar scenario of spin canting can account for the evolution of μ_{Cr} with annealing, as studied in this work for the $x = 0.15$ case (see Fig. 4d of main text). As shown in Fig. 6a, the difference between the calculated

and experimental differential cross sections increases linearly with the clustering tendency, monitored by the ASRO function $S(0) = S(K = 0) = 1 + \sum_i z_i \alpha_i$ (see Eq. 7 of main text). In fact, it is natural to assume an increase of θ with Cr clustering, owing to an increased magnetic frustration. This leads to a better agreement between the μ_{Cr} determined experimentally and the ones calculated by DFT (GGA), a shown in Fig. 5 and 6.

C. Limits of validity of the model

The expressions of the neutron cross sections derived in the main text (sections IIB) are valid for a collinear ferromagnetic alloy such as $Fe_{1-x}Cr_x$, but the case of an AF impurity state with respect to the average matrix is indeed covered and reflected by the negative sign of the average impurity moment. The main assumption of the model is that magnetic perturbations add linearly, which is true when local environments do not interact. This is the case of the studied alloys ($x \leq 0.15$) when one considers the near neighbor shells. The second assumption is that atomic short range order (ASRO) is a perturbation to the case of a random alloy.

The extension from colinear to canted states made here (summarized in section IVB of the main text) also assumes a linear additivity of the perturbations and weak ASRO. Namely, it mostly applies to dilute alloys. Canted or spin-glass local environments around an impurity state are also covered, in the simplest case where the impurity and its neighbor matrix moments are randomly canted. The random canting gives rise to a transverse magnetic cross section which is analogous to that of a paramagnetic sample. It behaves as an additional contribution to incoherent scattering if one neglects the K-dependence of the magnetic form factor, which yields a 10 -15% decrease of the magnetic scattering in the studied K-range for $3d$ alloys. A further extension to non-random canting could be easily developed, yielding modulations of this transverse cross section with the scattering vector. It is not considered in the present work, since this effect was not observed within the experimental accuracy.

For concentrated binary solid solutions, the models described above for collinear and canted local environments remain valid at zero order, when one considers only the average cross section or its K-dependence of the magnetic cross sections with the magnetic form factor. In such case the most important quantities, namely the average moments of the two constituents, can still be obtained quantitatively. This is an important advantage of neutron diffuse scattering with respect to other techniques.

[1] K. D. Rouse and M. J. Cooper Act. Cryst. A, **26**, 682 (1970).
[2] A. W. Hewatt, Act. Cryst. A, **35**, 248 (1979).
[3] I. A. Blech and B. L. Averbach, Phys. Rev. **137**, A1113 (1965).
[4] A. T. Aldred, Phys. Rev. B **14**, 219 (1976).
[5] T. P. C. Klaver, R. Drautz, M. W. Finnis, Phys. Rev. B. **74**, 094435 (2006).
[6] B. Drittler, N. Stefanou, S. Blugel, R. Zeller, P. H. Dederichs, Phys. Rev. B **40**, 8203 (1989).
[7] W. Marshall and S. W. Lovesey, *Theory of thermal neutron scattering*, Oxford Clarendon Press (1971).
[8] W. Marshall, J. Phys. C. **1**, 88, (1968).
[9] F. Gautier, Ann. Phys. **8**, 251 (1973).
[10] A. V. Ruban, P. A. Korzhavyi, B. Johansson, Phys. Rev. B **77**, 094436 (2008).